Corrosion and stress corrosion cracking resistances of the 17-4 precipitation hardened martensitic stainless steel additively manufactured using binder jet printing

Yida Xiong [a], Jayaraj Radhakrishnan [a], Sheng Huang [a], Yusheng Chua [a], Wei Shi [a c], Upadrasta Ramam urty [a b]

[a]

School of Mechanical and Aerospace Engineering, Nanyang Technological University, Singapore 639798, Republic of Singapore

[b]

Institute of Materials Research and Engineering (IMRE), Agency for Science, Technology and Research (A∗STAR), 2 Fusionopolis Way, Innovis #08-03, Singapore 138634, Republic of Singapore

[c]

Guizhou Key Laboratory of Materials Mechanical Behavior and Microstructure, College of Materials and Metallurgy, Guizhou University, Guiyang 550025, China

Abstract

The corrosion and stress corrosion cracking (SCC) properties of an additively manufactured (AM) 17-4 PH martensitic stainless steel that was produced using the binder jet printing (BJP) technique are compared with those of the conventionally manufactured (CM) steel, to critically examine the influence of porosity and subtle microstructural variations, introduced due to sintering and hot isostatic pressing (HIP), on them. Microstructures of the BJP and HIP specimens contain porosity, δ-ferrite, and MnS inclusions, while the CM ones do not contain either, but have NbC inclusions. All the corrosion properties of the BJP alloy, investigated using the immersion, cyclic potentiodynamic polarization, and galvanostatic (GL) tests, are inferior (compared to those of the CM alloy) due to the porosity in it, while the NbC inclusions present in the CM alloy adversely affected its corrosion characteristics. Surprisingly, the CM 17-4 PH specimens subjected to the SCC tests failed, while those of the BJP specimens did not (despite the relatively large porosity in it). Detailed analyses (including the X-ray computed tomography) show that crack bridging induced by the δ-ferrite phase, which has superior corrosion resistance compared to the martensite, is the reason for the BJP alloy's SCC resistance. HIP, which reduces both the porosity and δ-ferrite content, resulted in enhanced corrosion and SCC resistances that are even superior to those of the CM 17-4 PH. These results demonstrate, emphatically, that the subtle microstructural variations in the AM alloys can have profound effects on their properties, especially those related to structural integrity and reliability.

Graphical abstract

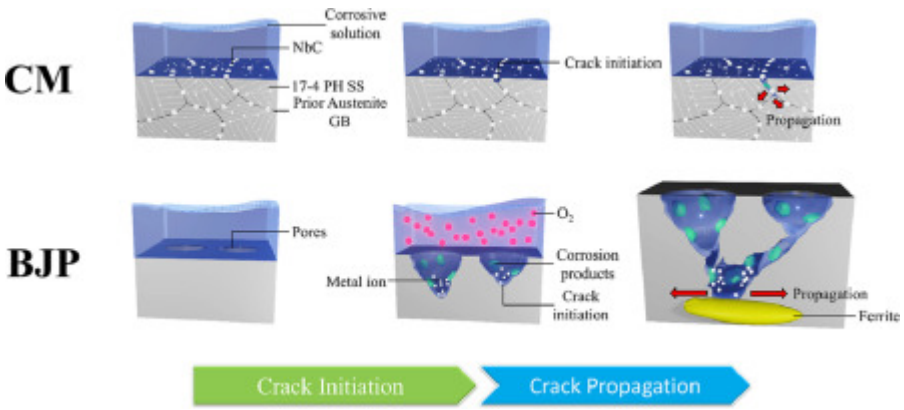

Keywords

Stainless steel
Corrosion
Stress-corrosion cracking
Ferrite
Additive manufacturing

1. Introduction

Additive manufacturing (AM) of metallic structural components has gained considerable attention in the recent past, due to the several advantages it offers as compared to conventional manufacturing (CM) [[1], [2], [3]]. The microstructures—and hence the mechanical properties—of the AM alloys, produced using techniques such as laser powder bed fusion (LPBF) and directed energy deposition (DED), are distinct, due mainly to the inherent conditions of rapid solidification and repeated thermal cycles that the alloy experiences upon solidification [[1], [2], [3]]. Consequently, considerable research efforts are being made to establish the processing-structure-property correlations in them. On the other hand, the microstructures in the alloys produced using the binder jet printing (BJP) appear similar (with equiaxed grains)—*prima facie*—to those of CM alloys. The BJP technique employs a liquid-based polymeric binder to produce 'green parts' from the metal/alloy powders. The green parts are then sintered to remove the binder and induce densification. The high homologous temperatures employed for sintering result in equiaxed microstructures, which, in turn, impart isotropic mechanical performance when compared to the other AM methods [[4], [5], [6]]. However, the parts manufactured with the BJP technique often exhibit relatively high porosity (even in those where the processing conditions are fine-tuned), often greater than 1% [[7], [8], [9]]. (For comparison, porosity in the parts manufactured using LPBF and DED could be less than 0.1 %). Such high porosity levels, which can adversely affect the BJP parts' mechanical [8,10,11] and corrosion properties [[12], [13], [14], [15], [16], [17], [18]], often mandate the use of a post-sintering hot isostatic pressing (HIP) step for minimizing the porosity [10,11].

Although the microstructures in the sintered BJP parts appear similar to their CM counterparts, subtle differences do exist [10,11]. HIP could also result in such microstructural variations. A detailed understanding as to how such variations—coupled with the porosity that is inherent—affect the performance of the components produced (in terms of not only the mechanical properties, but also functional attributes such as corrosion resistance, for example) is imperative. In this paper, we illustrate this aspect through the study of the corrosion and stress corrosion cracking (SCC) resistances of the 17-4 precipitation hardened (PH) martensitic stainless steel (MSS)—a highly suitable alloy for BJP. The PH MSSs offer an optimum combination of strength and ductility, which is attained by controlling the size and volume fraction of the Cu nano-precipitates through the ageing treatments, and excellent corrosion resistance [1,19,20]. As a result, they are widely used as structural materials, especially in corrosive environments that prevail, for example, in offshore platforms, water turbines, chemical industries [1,19,21,22]. The 17-4 PH MSS (simply referred to as 17-PH here afterwards) is the most popular grade amongst these steels. It typically contains 15-17.5 wt.% Cr and 3-5 wt.% Ni [23]. In addition to precipitation hardening, tempering treatment that introduces thin austenite layers within the microstructure can be employed to improve 17-4 PH's fracture toughness [2–4]. Depending on the heat treatment schedule, minor fractions of δ-ferrite can also be present in the microstructure of CM 17-4 PH [19,20,[24], [25], [26]]. In the peak aged condition (referred to as 'H900' in literature on the basis of the temperature (900 F) employed for ageing), the alloy has maximum strength, but relatively lower ductility [10,11].

Recently, we examined the microstructures and the mechanical properties (tensile, fracture toughness, unnotched fatigue, and fatigue crack growth, all at room temperature and in ambient conditions) of BJP 17-4 with different levels of porosity and in two different aging conditions (H900 and H1150) and compared them to those of CM 17-4 PH [10,11]. Results show that optimizing the printing parameters, for increasing the relative density of the final part, also affects the grain size as well as the δ-ferrite fraction. While the yield and tensile strengths of BJP 17-4 PH in the H900 condition are comparable to the respective properties of the CM alloy (also in the H900 condition), neither the porosity nor the δ phase fractions were found to exert any influence the strain hardening behaviour. HIP not only reduced the porosity and δ-ferrite fraction, but also refined the microstructure by inducing dynamic recrystallization. As a result, a substantial improvement in the unnotched fatigue strength, in addition to the improvements in quasi-static tensile strength and ductility, was noted.

In the present paper, we build further on our prior work, mentioned above, with a view to critically examine the following aspects. (i) Both BJP and HIP 17-4 contain notable amounts of porosity and δ-ferrite in their microstructures. While both of these are undesirable in 17-4 PH, from the mechanical properties point of view [11,27,28], to what extent they affect the corrosion and SCC resistances requires a close examination. This is particularly critical for ascertaining the suitability of the structural components of BJP 17-4 PH in corrosive environments. (ii) Both the sintering and HIP steps can also affect the size and volume fraction of inclusions such as MnS and NbC in BJP 17-4 PH, which are likely to affect its corrosion and SCC characteristics. (For example, it is well known that the presence of MnS in stainless steels can initiate pitting [19,[29], [30], [31], [32], [33]]). The interplay between such inclusions and the microstructural variations mentioned in (i) in affecting the corrosion and SCC resistances needs a critical evaluation. (iii) As already mentioned, the microstructures of BJP and CM alloys are similar, resulting in the general belief that their performances (both mechanical and functional) are also likely to be similar. However, the subtle differences that exist could play a major role in dictating the properties, especially those aspects that are critical for ensuring structural integrity over a long period of service (such as SCC and fatigue resistances). For example, Kumar et al. [34]'s work on the BJP 316L austenitic stainless steel showed that its unnotched fatigue strength, in spite of the presence of considerable porosity in it, is comparable to that of CM 316L. This was shown to be a result of the unique microstructural features that render the short cracks that nucleate during the cyclic loading get deflected and arrested. Since the SCC resistance is also critical aspect for ensuring structural integrity of load bearing components in corrosive environments, it is instructive to examine the role of subtle microstructural differences induced during the BJP process (namely, sintering and HIP if applicable) on it.

2. Materials and experiments

The corrosion and SCC resistances of 17-4 PH (in the H900 condition) that was processed using three different methods were examined in this study. As already mentioned, processing, microstructures, and room temperature tensile properties, fracture toughness, and fatigue crack growth resistances of them were already reported by us [10,11]. Therefore, we briefly provide key details for the sake completeness here (details can be found in [10,11]). The CM specimens were machined from commercially available hot-rolled plates, which were solutionized at 1040 °C for 2 h. For the other two types of specimens, commercially available pre-alloyed 17-4 PH steel powders were employed for manufacturing several cuboid blocks (10 mm by 10 mm cross-section and 70 mm height) using a Metal Binder Jet printer (HP Inc, Corvalis, USA) that utilizes a water-based liquid binder. The green parts (~50–60% relative density [35]) were sintered at a temperature of 1370 °C for 2 h in a hydrogen

atmosphere. The porosity (f_ϕ), evaluated using the Archimedes principle, in the as-sintered specimens is ~ 3.3 ± 1 %, which is relatively high. The pore size (expressed as the square root of the pore's cross-sectional area), is also large (maximum pore size reached ~ 315 µm, with the pore size distribution detailed in Fig. S1 (referred to as "batch A") in the supplementary document.) [10]. Keeping this in view, some BJP specimens are subjected to HIP at 1160 ± 10°C with an applied pressure of 104 MPa for 4 h in an Ar atmosphere (1040°C/2 h). As expected, HIP led to a substantial reduction in both f_ϕ (~0.76 to 1.18%) and the pore size (maximum pore size reduced to ~25 µm, with the pore size distribution detailed in Fig. S1 (referred to as "batch A+HIP") in the supplementary document.) [10]. Both the as-sintered and HIP specimens (referred to as BJP and HIP, here afterwards) were solutionized at 1040°C for 2 h to dissolve any precipitates that might have formed during sintering and/or HIP steps and minimize the δ – ferrite phase formed during the sintering process. Lastly, all the CM, BJP, and HIP specimens were age-hardened to the H900 condition: 482°C for 1 h, following the AMS 2759/3J standard [36]. The chemical compositions of the CM, BJP, and HIP specimens are given in Table 1.

Table 1. Compositions (in wt.%) (major elements) of CM, BJP and HIP specimens.

Specimen	Fe	Cr	Ni	Cu	Nb	Mn	Si
CM	73.5	16.2	4.5	3.2	0.3	0.7	0.4
BJP	72.0	17.1	4.3	3.7	0.2	0.8	0.8
HIP	71.3	16.9	4.3	3.9	0.2	0.9	1.0

Microstructural observations, including baseline and morphology assessments of the corrosion products and cracks (induced during the SCC experiments) across different specimens, were carried out using a JEOL 7800F Prime field-emission scanning electron microscope (SEM). Backscattered electron (BSE) imaging, electron backscatter diffraction (EBSD), and energy-dispersive X-ray spectroscopy (EDS), all integrated into this SEM, were employed to determine grain morphologies, phase and elemental distributions within the microstructure. Additionally, X-ray computed tomography (XCT) was performed using the Xradia CrystalCT (Zeiss, Germany) to image the cracks and their interactions with the microstructural features in various SCC-tested specimens in 3D. The operating voltage was set to 160 kV with the HE4 filter provided with the machine. The commercially available software DragonFly was used for the 3D reconstruction and analysis, with the scan data reconstructed into isotropic cubes with a side length of 1.54 µm.

Microstructure and local compositional analysis of specific locations, such as the ferrite/martensite interfaces, was performed using scanning transmission electron microscopy (STEM) in a JEOL 2100F/ARM 200F transmission electron microscope. The samples utilized for the STEM characterization were produced using the Zeiss Crossbeam 540 focused ion beam (FIB) milling. Coarse milling (30 kV, beam current: 30 nA to 15 nA) was initially adopted to lift the lamella out. During the thinning of the lamella, the beam current was reduced step by step, following the usual procedures for this process. The final thinning of the lamella was conducted at 2 kV and 10 pA to remove any amorphous layer formed during the previous thinning processes.

The corrosion properties of the alloys were investigated using the immersion, cyclic potentiodynamic polarization, and galvanostatic (GL) tests on specimens with 10 mm × 10 mm × 5 mm dimensions. One of the 10 mm × 10 mm surfaces of each specimen was ground sequentially using #800, #1200, #2400, and #4000 silicon carbide papers, and then polished with 3 and 1 µm diamond powder pastes.

All the other non-polished surfaces were coated with epoxy prior to the corrosion tests. In the immersion tests, the specimens were submerged in a 3.5 wt% NaCl solution for 10 days. Afterwards, the corrosion initiation sites were characterised using various techniques. For the cyclic potentiodynamic polarization tests, a classic three-electrode cell was employed. Specimens were initially immersed in a 3.5 wt% NaCl solution for 2 h to stabilize the open-circuit potential (OCP). The tested specimen served as the working electrode, while a silver/silver chloride (Ag/AgCl) electrode (E= +197 mV vs. Standard Hydrogen Electrode (SHE)) was utilized as the reference electrode, and a graphite electrode functioned as the counter electrode. The scan was initiated from -0.5 V vs. (Ag/AgCl) electrode towards the anodic direction, with a scan rate of 0.167 mV/s. Upon reaching a current density of 1 mA/cm^2, the scan direction was reversed. The test concluded when the cathodic current density reached -1 mA/cm^2. For the GL tests, the same three-electrode cell was employed. Guided by the cyclic potentiodynamic results, a current density of 0.1 mA/cm^2 was chosen for the GL tests to facilitate stable growth of the localized corrosion products. These tests were performed in the 3.5 wt% NaCl solution and for a duration of 10 minutes. To assess the protectiveness of the oxide film, electrochemical impedance spectroscopy (EIS) was conducted using the same three-electrode cell setup in a 3.5 wt% NaCl solution. The EIS measurements were taken at OCP over a frequency range of 100 kHz - 10 mHz, with a signal amplitude of 10 mV (rms). Two specimens were tested for each manufacturing condition in all the above corrosion experiments.

The SCC tests were carried out on specimens with a gauge length four times the diameter (gauge length: 14 mm, diameter: 3.5 mm) in a 3.5 wt% NaCl solution, as outlined in the ASTM E8/E8M standard [37]. Each specimen was subjected to the same constant load (950 kgf) that results to an initial tensile stress (968 MPa), which corresponds to 90% of the yield stress (σ_y) of the BJP specimen (σ_y = 1079 MPa). Note that the σ_y of the CM and HIP specimens are higher (1173 and 1228 MPa, respectively [10]. Additionally, SCC tests with an initial tensile stress of ~700 MPa, which corresponds to 65% of σ_y of the BJP specimen were also performed. These tests will subsequently be referred to as the "90% YS SCC" and "65% YS SCC" tests, respectively. (Such constant load tests are widely employed for evaluating the SCC resistance of alloys. The lifetimes assessed with them contain both the crack initiation and propagation phases, which is particularly suitable in the current context, since our interest is to examine the effect of porosity, which is likely to reduce the time required for initiating a critical crack substantially, on SCC resistance of the BJP alloys.) In each SCC test, the solution was pumped into the test chamber after the load was applied, such that the entire specimen is immersed in the solution. Each cycle consisted of 10 minutes of immersion, followed by 50 minutes of dry condition. If the specimen did not fail within 90 days, it was declared as 'run out'. In some instances, SCC in 17-4 PH can occur under cathodic protection [38,39]; this aspect is not pursued in this study, but will be examined in future.

A Dimension Icon scanning probe microscope (Bruker, USA) was used to measure the Volta potentials of the martensite and ferrite. Specimens for these measurements were initially ground and final polished with 1 μm diamond powders, before finishing with an OP-U suspension. Since the hardness of martensite is significantly higher than that of ferrite, the ferrite exhibits a lower protrusion, compared to the surrounding martensite, after such preparation of the specimens. In these scanning Kelvin probe force microscopy (SKPFM) tests, a bias voltage was applied to the probe, resulting in a measured Volta potential difference between the specimen and the probe. The primary scan captured the topographic image. After that, a second scan was performed to measure the Volta potential. These experiments were performed with the following parameters: resolution of 256 × 256, scanned area of

50 × 50 μm^2, scan frequency of 0.996 Hz. The experimental data was analysed and processed using the NanoscopeV8.1x software.

3. Results

3.1. Baseline microstructure

The inverse pole figures (IPFs) of the CM, BJP, and HIP specimens are displayed in Fig. 1(a_1, b_1, c_1), respectively. The prior austenite grains were reconstructed by transforming the martensite using the Kurdjumov-Sachs orientation relationship, as shown in Fig. 1(a_2, b_2, c_2), respectively. The phase maps of these specimens, shown in Fig. 1(a_3, b_3, c_3), indicate that in all the three types of specimens examined, the microstructure predominantly (more than 99%) consists of the body centered cubic (bcc) phase. The prior austenite grain sizes of the CM, BJP, and the HIP specimens are 64 ± 10, 77 ± 19 μm, and 28 ± 10 μm, respectively [10]. The respective EDS maps of the Cr and Ni elements obtained are shown in Fig. 2. In the BJP and HIP specimens, Cr-enriched, Ni-depleted, skeleton-like phases, which correspond to δ-ferrite [11], were observed. In contrast, the CM specimens appear devoid of δ-ferrite. The estimated values of the δ-ferrite area fractions in the CM, BJP, and HIP specimens are ~ 0%, 21.4 ± 1.7 %, and 6.2 ± 0.7 %, respectively [10,11]. (These were determined through optical microscopy on polished and etched (using Kalling's reagent (2 g $CuCl_2$, 40 ml HCl, and 80 ml C_2H_5OH) samples.) While the HIP process led to a substantial reduction in the δ-ferrite fraction, in comparison to that in the BJP specimens, it is still a higher than that of the CM specimens. The HIP process also transformed the morphology of the δ-ferrite from a skeleton-like to an island-like [10].

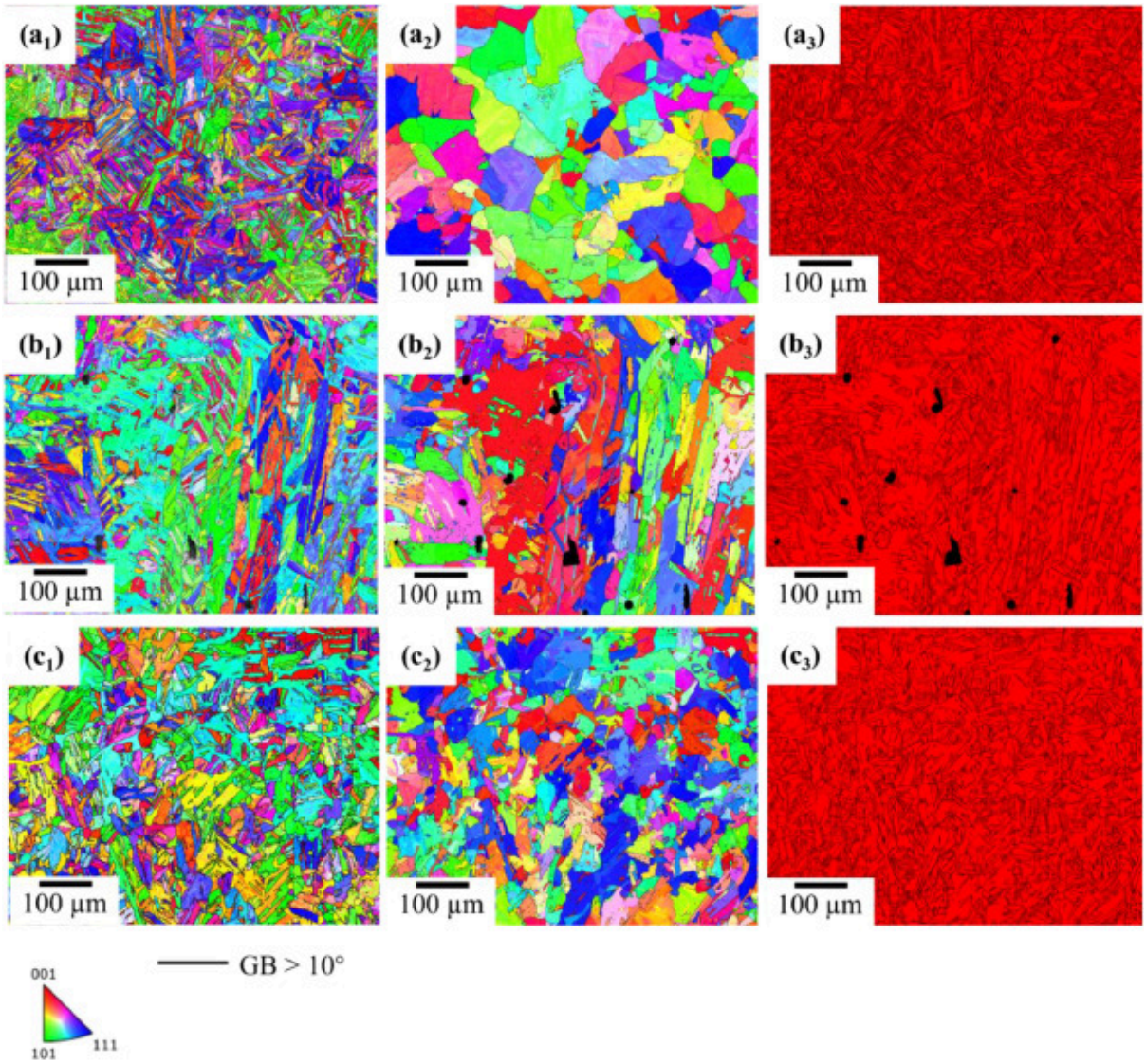

1. Download: Download high-res image (3MB)
2. Download: Download full-size image

Fig. 1. EBSD analyses of the CM (a_1, a_2, a_3), BJP (b_1, b_2, b_3), and HIP (c_1, c_2, c_3) specimens: grain orientation maps (a_1, b_1, c_1) and their respective reconstructed prior austenite grain maps (a_2, b_2, c_2) with IPF coloring; in the phase maps (a_3, b_3, c_3), red represents the “bcc” structure and blue represents the “fcc” structure.

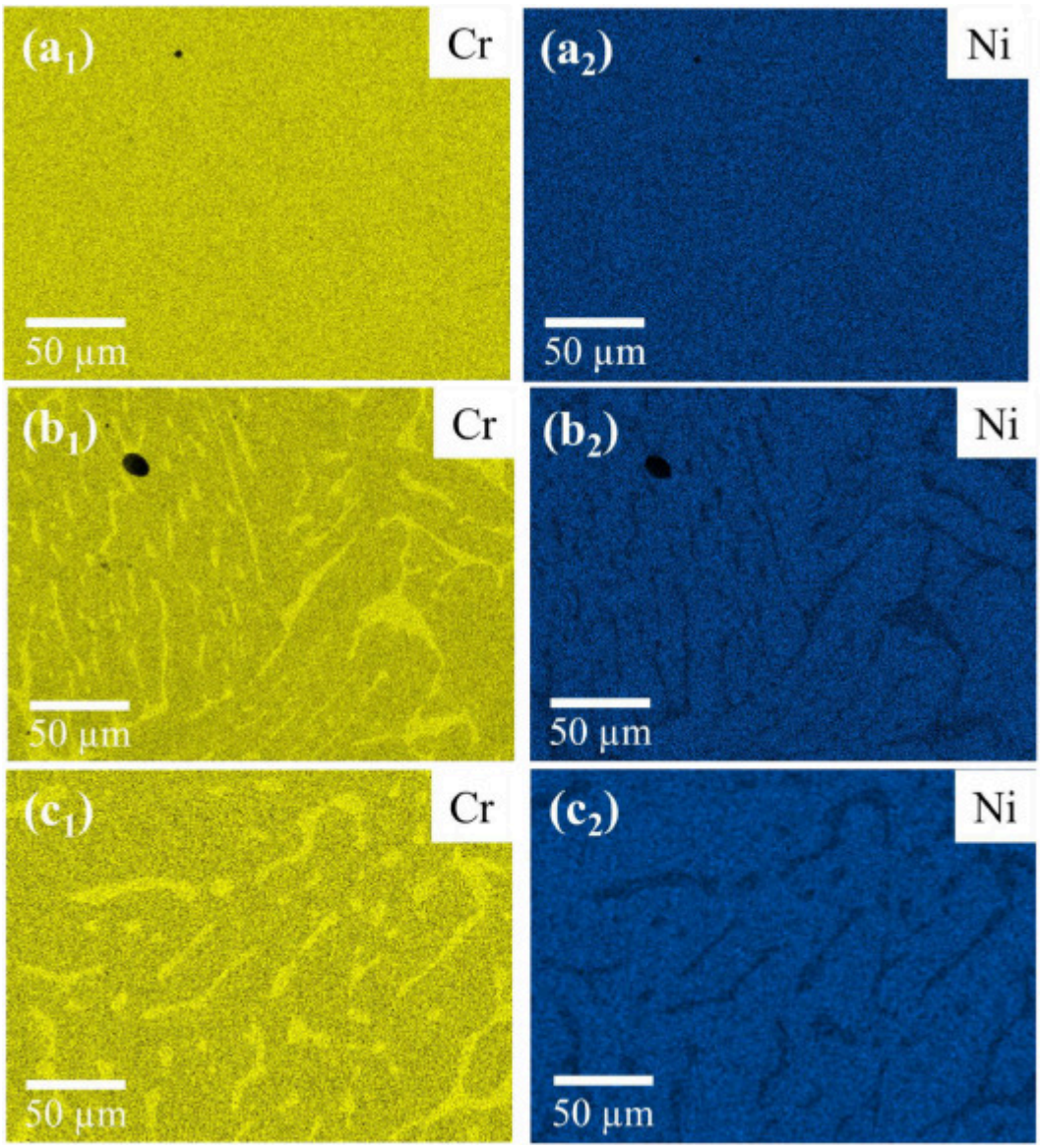

1. Download: Download high-res image (3MB)
2. Download: Download full-size image

Fig. 2. δ-ferrite distribution in the CM (a_1, a_2), BJP (b_1, b_2), and HIP (c_1, c_2) specimens: EDS maps showing the distribution of Cr (a_1, b_1, c_1) and Ni (a_1, b_1, c_1).

The distribution of MnS inclusions in different specimens is shown in Fig. 3. In the CM specimens, they were not detectable (at the magnification level utilized during SEM). Some MnS particles were observed in both the BJP and HIP specimens. In contrast, NbC inclusions were prominently observed in the CM specimens, whereas they could not be detected in both the BJP and HIP specimens (Fig. 4). BSE imaging, employed for this analysis, identified these inclusions as bright spots, in agreement with outcomes from previous studies [[40], [41], [42], [43], [44]]. EDS point analysis further confirmed these bright spots as the NbC inclusions. (A detailed example of the NbC inclusion composition, as measured by EDS, is provided in the Table S1 in the supplementary document.).

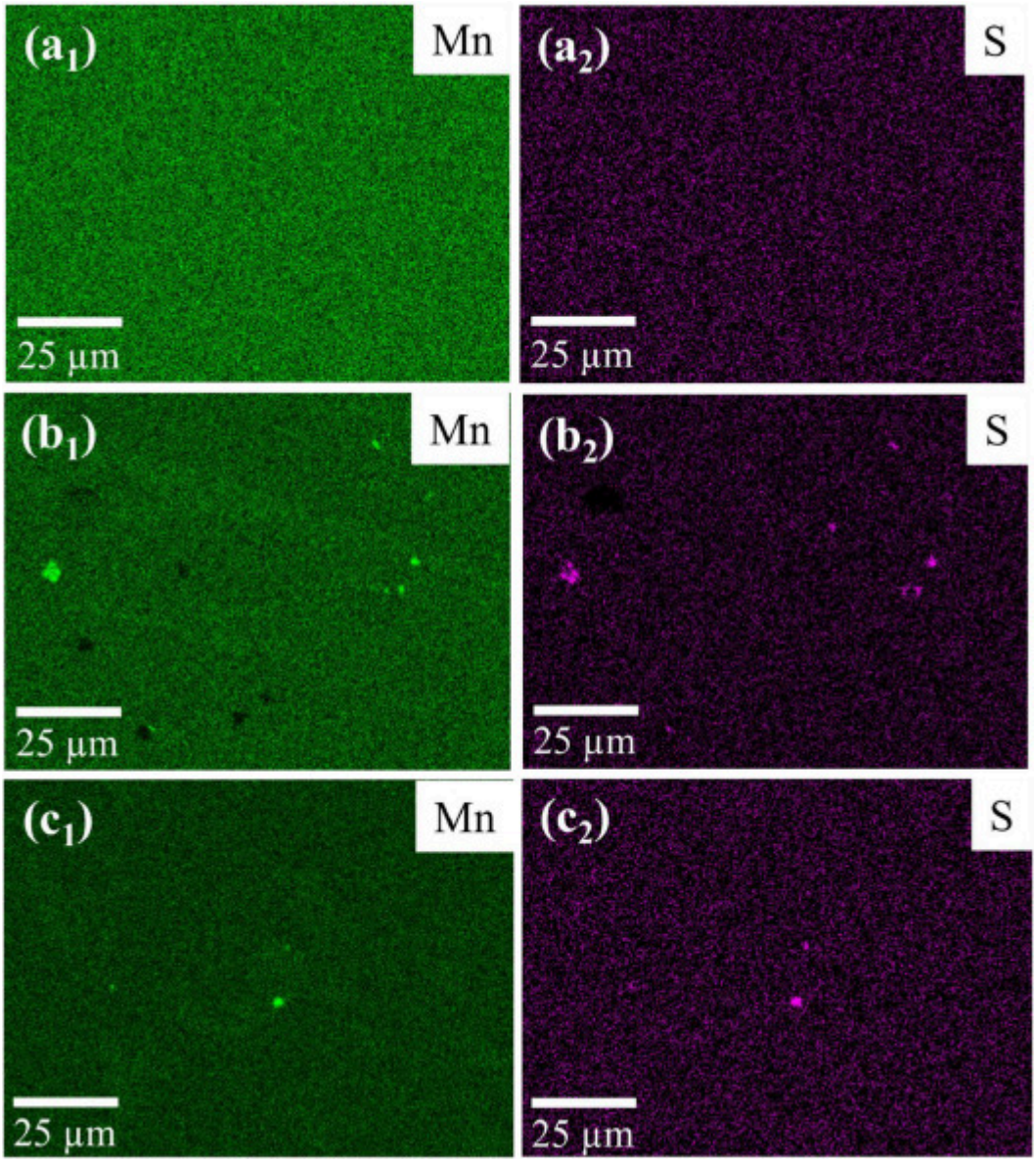

1. Download: Download high-res image (3MB)
2. Download: Download full-size image

Fig. 3. MnS distribution in the CM (a_1, a_2), BJP (b_1, b_2), and HIP (c_1, c_2) specimens: EDS maps showing the distribution of Mn (a_1, b_1, c_1) and S (a_1, b_1, c_1).

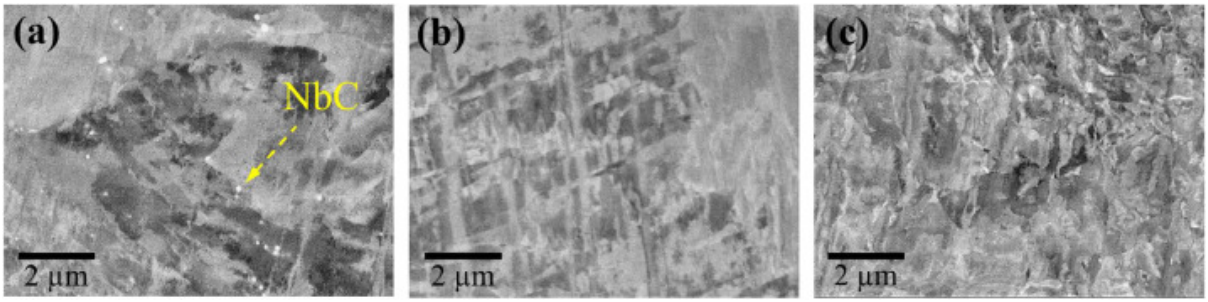

1. Download: Download high-res image (778KB)
2. Download: Download full-size image

Fig. 4. NbC distributions in the (a) CM, (b) BJP, and (c) HIP specimens

Corrosion along the ferrite/martensite interfaces and inside the ferrite phase in the HIP specimens was observed, which will be discussed later. Accordingly, both the ferrite boundaries and the δ-ferrite itself were analysed. Results of the STEM EDS analyses are displayed in Fig. 5(a_1-a_3, b_1, b_2). They show that the Cu-enriched particles are located inside the δ-ferrite and along the ferrite/martensite interface, which is consistent with the findings of prior studies [44]. Fig. 5(b_3) shows a Fast Fourier Transform (FFT) image of a location inside δ-ferrite (left) and a high-resolution STEM image of a location inside δ-ferrite (right). The STEM EDS line scans and maps, Fig. 5(a_2, a_3, b_1, b_2, d_1, d_2), reveal Cr depletion at the locations containing the Cu-enriched particles.

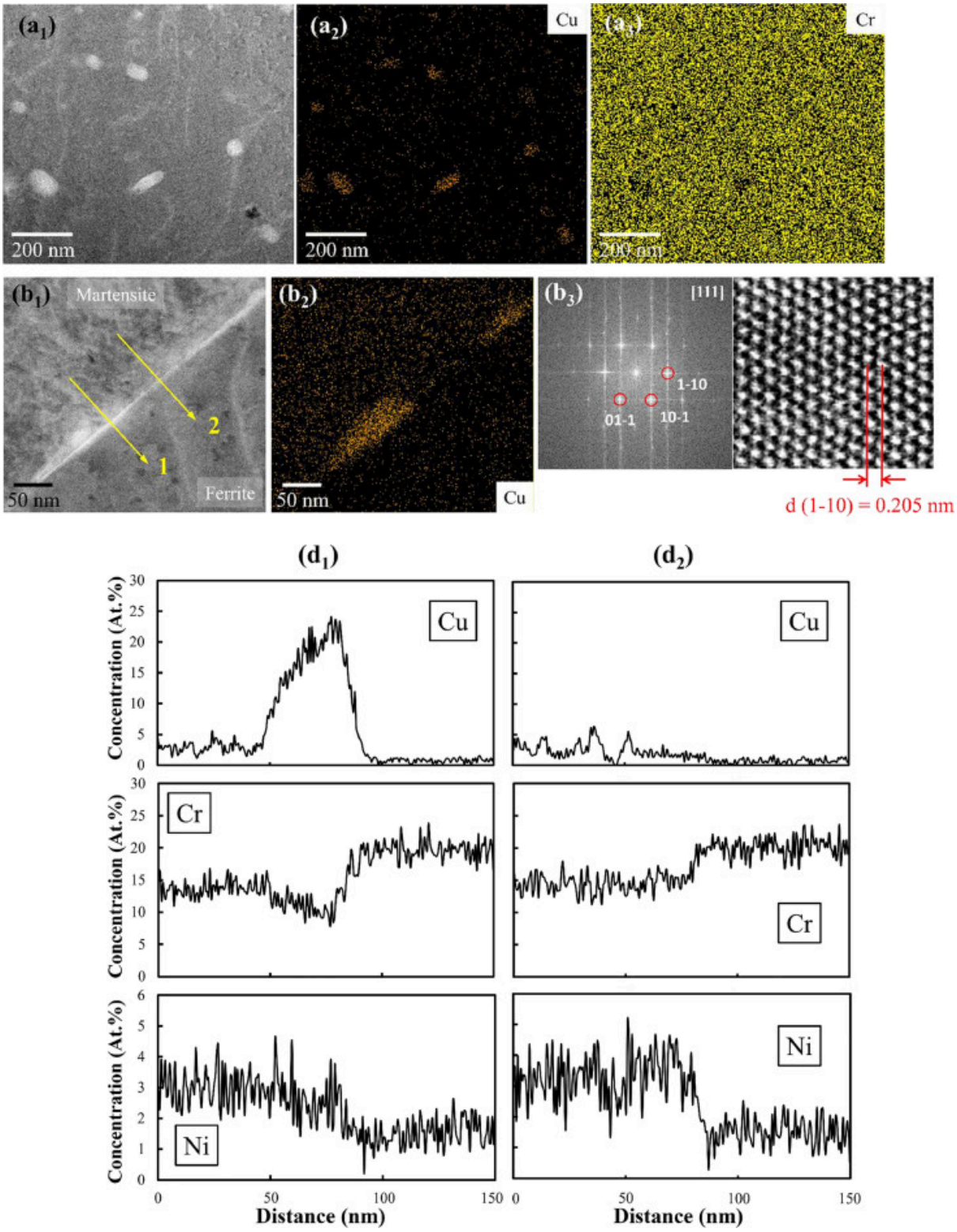

1. Download: Download high-res image (2MB)
2. Download: Download full-size image

Fig. 5. Analysis of the δ-ferrite: STEM image (a_1) and corresponding STEM EDS maps (Cu and Cr elements) (a_2, a_3) of one location inside the ferrite; STEM image (b_1) and corresponding STEM EDS map for Cu (b_2) around the ferrite/martensite interface; (c_3) FFT image of a location inside δ-ferrite (left) and High-resolution STEM image of a location inside δ-ferrite (right); composition profiles of line

scans 1 (d_1) and 2 (d_2) (corresponding to the yellow arrows shown in (c_1)).

The Volta potential, measured by using the SKPFM technique, is directly related to the electron escape work function (EWF). The Volta potential map in Fig. 6 clearly shows that the potential of ferrite is more positive than that of the martensite, indicating that the former is more noble [45]. A higher Volta potential in δ-ferrite has also been reported in [46]. Considering that chromium is the main element responsible for passivation in the stainless steels, it is logical to associate the higher EWF with the ferrite phase, which enhances corrosion resistance. The δ-ferrite in the BJP specimens also exhibits similar features.

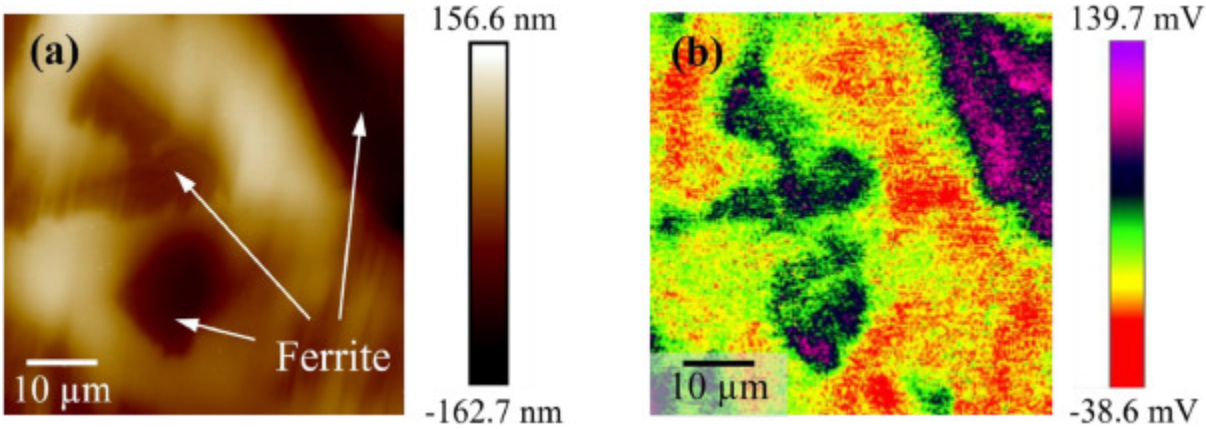

1. Download: Download high-res image (587KB)
2. Download: Download full-size image

Fig. 6. AFM analysis of a location containing both ferrite and martensite: (a) surface topography map and (b) the associated Volta potential profile.

3.2. Corrosion tests

Results of the immersion tests on the CM specimens are shown in the Fig. 7(a_1, a_2). The corrosion sites in them were identified at the NbC inclusions. Fig. 7(b_1-b_3) show the morphology of a pore in a BJP specimen, before and after the immersion test, respectively. It is evident from them that the pores cause severe corrosion during the immersion test. Internal corrosion within the pores was extensively observed in all the tested BJP specimens. A three-dimensional reconstructed view of one pore after an immersion test is shown in Video 1. In the HIP specimens, Fig. 7(c_1-c_2), corrosion was observed to occur discontinuously along the ferrite/martensite interface and inside the δ-ferrite. By comparison with the non-corroded specimens, it can be inferred that corrosion primarily occurred at locations with the Cu-enriched particles.

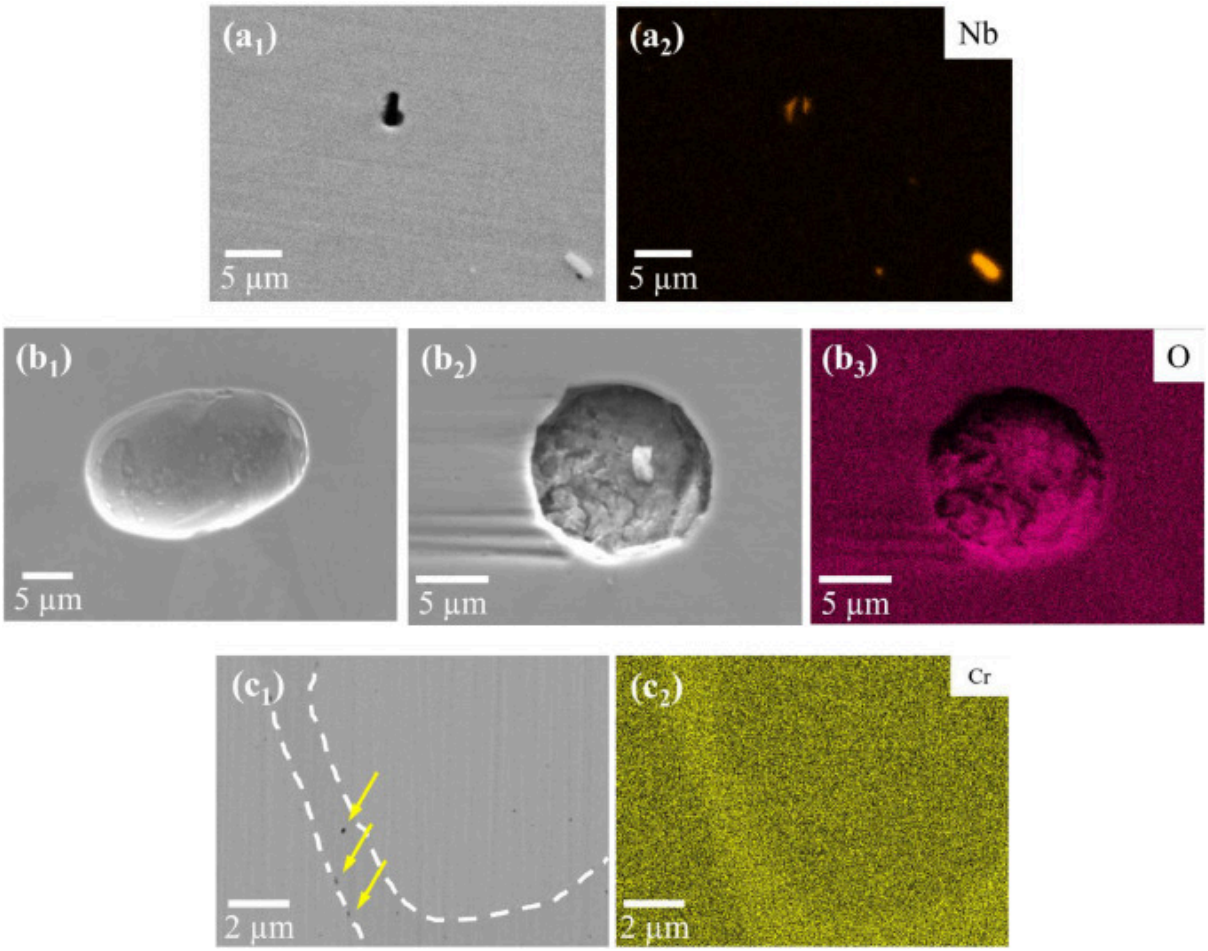

1. Download: Download high-res image (2MB)
2. Download: Download full-size image

Fig. 7. Representative immersion test results for CM (a_1, a_2), BJP (b_1-b_3) (with b_1 showing a pore before the immersion test), and HIP (c_1, c_2). Areas marked by white dotted curves in (c_1) indicate δ-ferrite. The yellow arrows in (c_1) indicate the corroded locations inside the δ-ferrite and along the ferrite/martensite interface.

SEM images obtained from the different GL tested specimens are presented in Fig. 8. It is observed that corrosion preferentially occurred around the NbC particles in the CM specimens, consistent with the immersion test results. In the case of the BJP specimens, mirroring the immersion test findings, pores experienced severe corrosion and tended to interconnect. In the HIP specimens, corrosion was identified at the ferrite/martensite interface. In the BJP and HIP specimens, corrosion was also observed around the MnS inclusions in the immersion and GL tests, and the corresponding results are shown in Figs. S2 and S3 in the supplementary document.

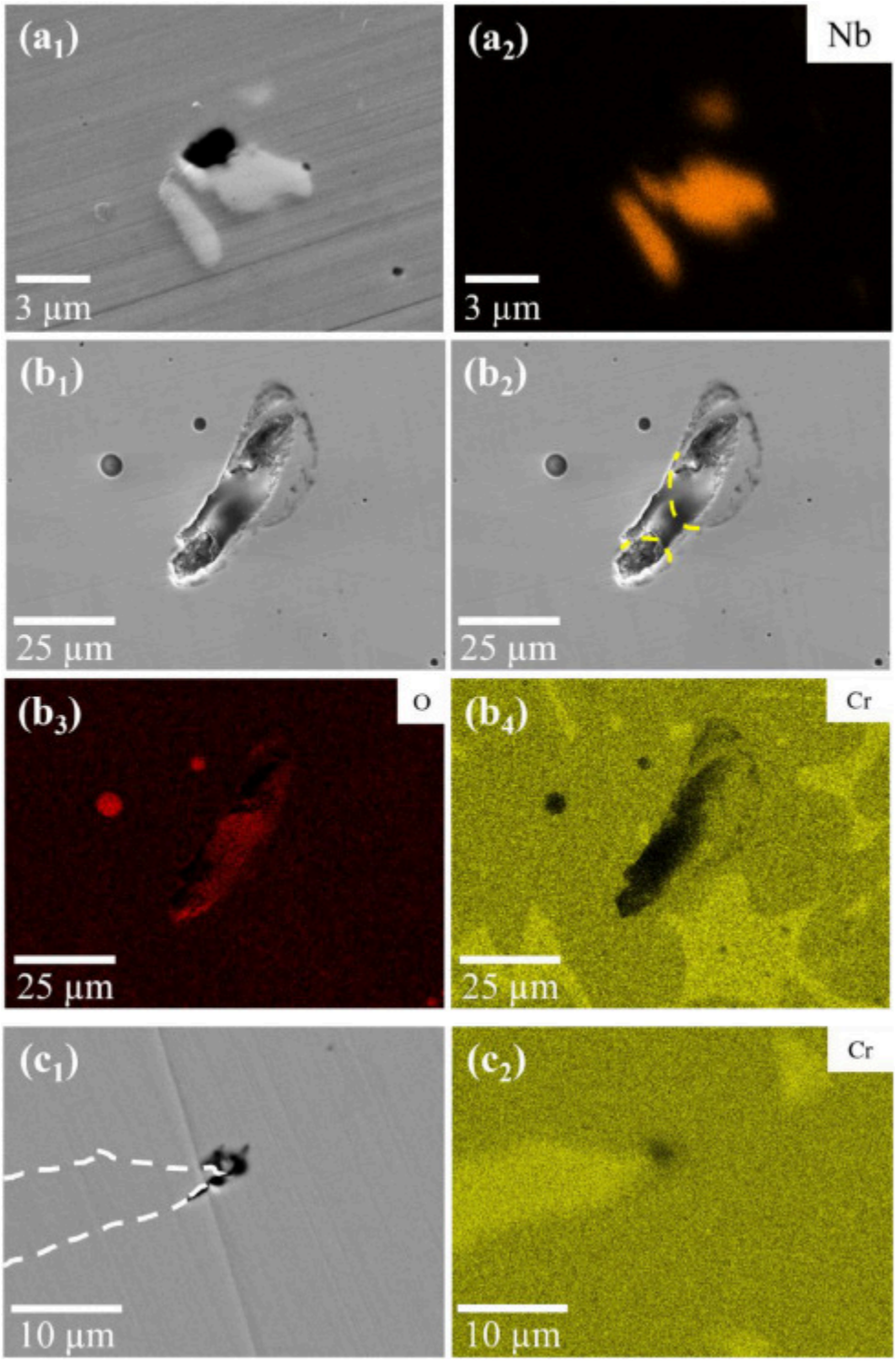

1. Download: Download high-res image (2MB)
2. Download: Download full-size image

Fig. 8. Representative GL test results for CM (a_1, a_2), BJP (b_1-b_4), and HIP (c_1, c_2). The yellow dotted lines in (b_2) represent the original boundaries of the pores. Areas marked by white dotted curves in (c_1) indicate δ-ferrite.

Results of the cyclic potentiodynamic test are displayed in Fig. 9(a) and the key corrosion properties obtained from them are summarized in the Table 2. The BJP specimens exhibit a significantly higher corrosion rate, with a smaller passive window (the specimen is considered as passive when the

current density is less than 10 μA/cm^2 [19]), compared to the CM specimens. However, after HIP, the corrosion rate of the BJP specimens reduced to around half of that of the CM specimen, indicating the beneficial effects of HIP on the corrosion properties of the steel.

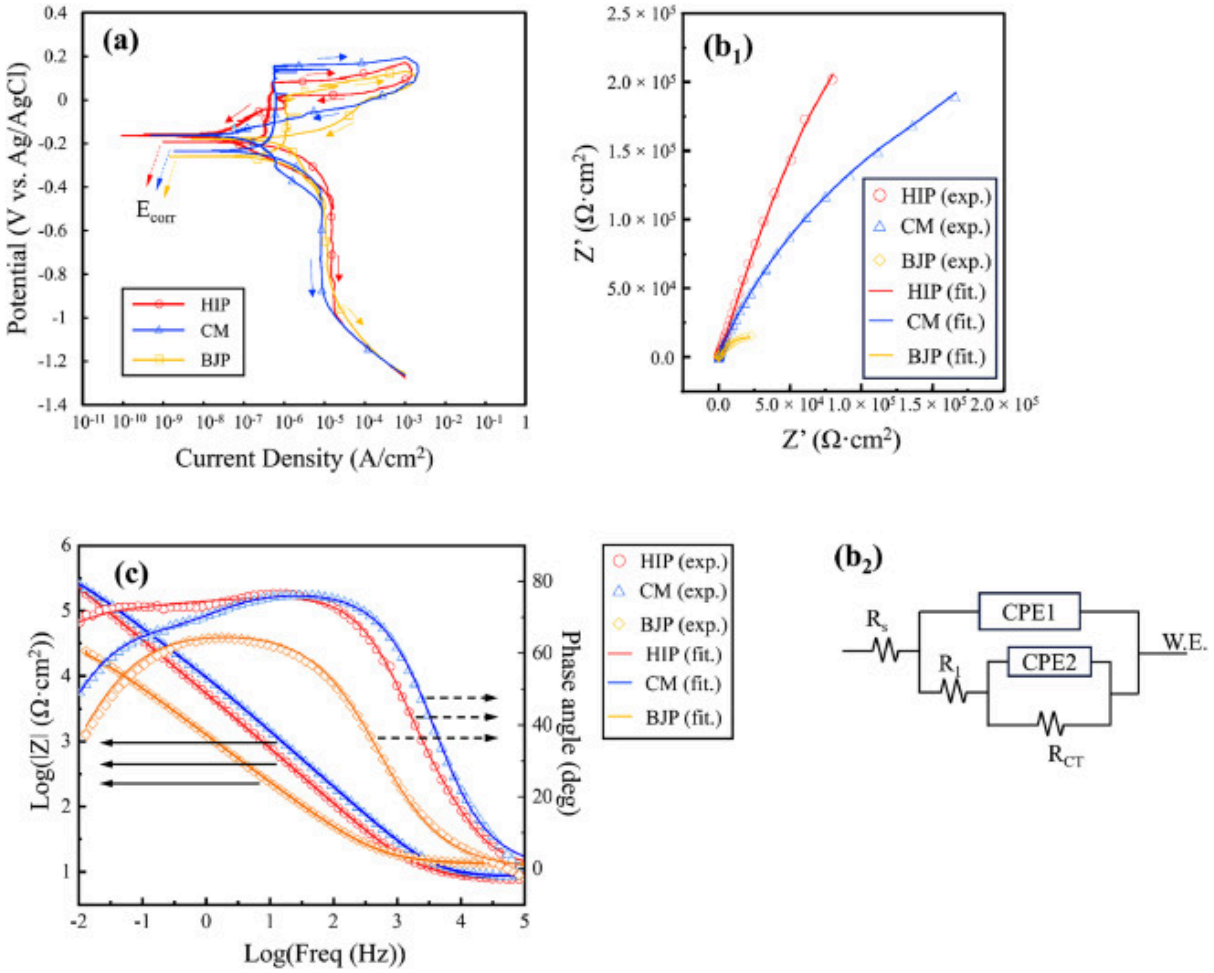

1. Download: Download high-res image (754KB)
2. Download: Download full-size image

Fig. 9. Electrochemical analyses. (a) results from cyclic potentiodynamic polarization tests; (b_1) EIS results presented in Nyquist plots (with the equivalent circuit diagram used for data fitting shown in (b2), and (c) the Bode plots. Note that "exp." refers to experimental data, and "fit." denotes the fitted curves.

Table 2. Results of the cyclic potentiodynamic tests.

Specimens	Corrosion rate(A/cm^2)	Passive current density(A/cm^2)	Corrosion potential (vs. Ag/AgCl) (V)	Pitting/Breakdown potential (vs. Ag/AgCl) (V)
CM	~5.4 × 10^{-7}	~6.3 × 10^{-7}	~ -0.17	~ 0.16
BJP	~1.1 × 10^{-6}	~1.2 × 10^{-6}	~ -0.23	~ 0.03
HIP	~2.8 × 10^{-7}	~3.7 × 10^{-7}	~ -0.26	~ 0.08

The Nyquist and Bode plots, obtained from the EIS analyses, are displayed in Fig. 9(b_1, b_2 and c), respectively. The equivalent circuit of the oxide film under all the conditions is shown in Fig. 9(b_2). In it, R_s is the solution resistance, R_{CT} is the charge-transfer resistance of the Faraday processes, CPE2

is the constant phase element of the electric double layer, R_1 is the resistance of the oxide film, and CPE1 is the constant phase element for the oxide film. The fitting parameters for the equivalent circuit are summarized in Table 3, where Y_0 and *n* are the characteristic parameters of the constant phase element, and the χ^2 is the goodness of fit. Results show that R_1 of the HIP specimens are significantly larger than those of the other two. In contrast, the low-frequency impedance and phase angle of the BJP specimens are lower, compared to the CM and HIP specimens. Additionally, the Y_0 of CPE1 for BJP is notably greater than that of the other two. These findings indicate the oxide film's protectiveness increases in the following order: BJP (least protective), CM, HIP (most protective) [47,48].

Table 3. Fitting parameters of the equivalent circuit in Fig. 9 (b_2).

Specimen	R_S**(Ω·cm²)**	**CPE₁**		R_1 **(10⁴ (Ω·cm²))**	**CPE₂**		R_{CT}**(10⁶ (Ω·cm²))**	χ^2 **(10⁻³)**
		Y_0 **(10⁻⁶ S·sⁿ·cm⁻²)**	**n**		Y_0 **(10⁻⁶ S·sⁿ·cm⁻²)**	**n**		
HIP	7.98	37.58	0.85	9.85	7.01	0.80	1.92	1.10
CM	8.49	19.39	0.86	3.51	9.47	0.62	0.70	0.41
BJP	13.24	203.70	0.74	4.43	5.12	0.83	0.12	1.23

3.3. SCC tests

None of the BJP and HIP specimens subjected to either the 65% YS or 90% YS SCC tests failed, even after 90 days of testing (Some tests were let run up to 120 days, yet no failure occurred.) In contrast, the three CM specimens subjected to the 90% YS SCC tests failed after 37, 50 and 67 days, while the two subjected to the 65% YS SCC tests failed after 40 and 69 days. While the large variability in the failure times of the CM specimens is noteworthy, these results show unequivocally that the BJP and HIP specimens' resistance to SCC induced failure is far superior. This is surprising, given the level of porosity (especially in the BJP specimens) and the significantly lower corrosion resistances in BJP 17-4 (as presented in the preceding section). Detailed microstructural investigations were conducted to ascertain the mechanisms responsible for this surprising result. They are presented below.

An optical micrograph of a crack that was observed in the CM specimen that failed after 37 days is shown in Fig. 10(a_1). Fig. 10(a_2) and Video 3 show a 3D reconstruction of the crack (the crack is rendered in light blue for clear visualization and the grey part in the video represents the surrounding uncracked material) obtained via XCT. Fig. 10(a_3-a_6) show several sequential cross-sectional XCT images of the crack. The crack created due to the stress corrosion in the CM specimen is sharp and primarily propagated in a direction perpendicular to the loading direction, aligning with the plane of maximum normal stress (the aspect ratio of the crack is approximately 2.5). For comparison, an optical micrograph of a crack that was observed in the BJP specimen subjected to the 90% YS SCC test for 90 days (and did not fail) is shown in Fig. 10(b_1). Fig. 10(b_2) and Video 5 show a 3D reconstructed view of the crack (the crack is rendered in blue for clear visualization and the grey part in the video represents the surrounding uncracked material.). The results of the XCT scans performed on it, showcasing serial cross-sections containing the crack, are shown in Video 4. In this video, the brightness observed in XCT is directly correlated with the density of the scanned part. Several cross-sectional XCT images from these serial scans are presented in Fig. 10(b_3-b_6). Analysis of both the video and the figures reveals that the crack is blunt; importantly, it did not propagate predominantly perpendicular to the applied stress (the aspect ratio of the crack is approximately 0.7), unlike the sharp crack observed in the CM specimen. Inside the crack (Fig. 10(b_3-b_6) and Video 4), distinct

skeleton-like features that did not dissolve and appear to “bridge” the crack were detected, exhibiting a brighter intensity compared to the surrounding areas. Notably, these features closely resemble the Cr-enriched δ-ferrite phases, identified earlier by using EDS (Fig. 2(b_1, b_2)).

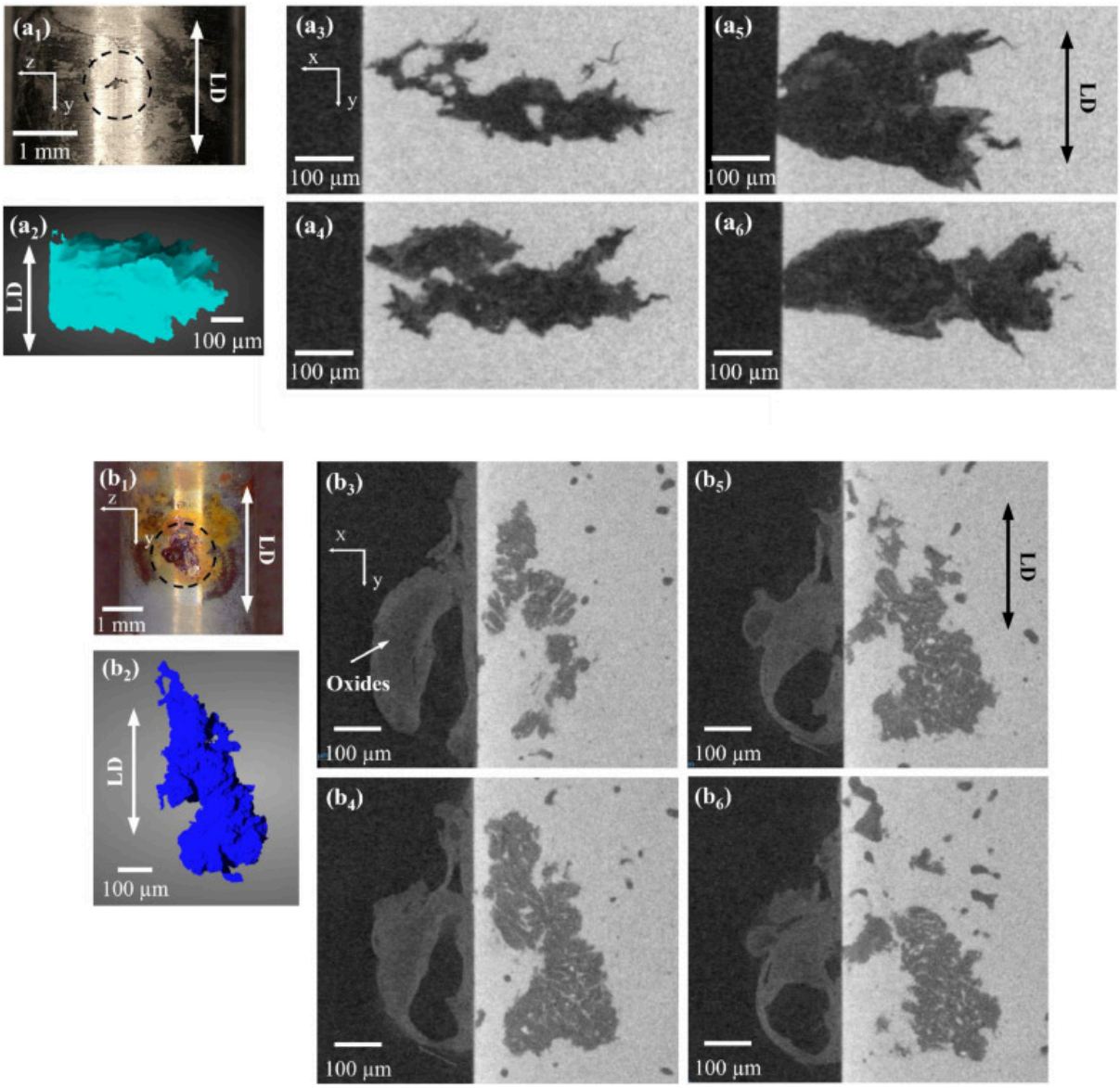

1. Download: Download high-res image (1MB)
2. Download: Download full-size image

Fig. 10. XCT analysis of cracks observed in the CM (a_1-a_6) and BJP (b_1-b_6) specimens: out part of a crack (marked by a black circle) observed in the CM specimen (optical micrograph) (a_1); 3D reconstruction (a_2) of the inner part of the crack in (a_1). XCT images (a_3-a_6) of the cross sections containing the crack in (a_1). out part of a crack (marked by a black circle) observed in the BJP specimen (optical micrograph) (b_1). 3D reconstruction (b_2) of the inner part of the crack in (b_1). (b_3-b_6) XCT images of the cross sections containing the crack in (b_1). "LD" stands for the loading direction. The x, y, and z axes shown in (a_1, a_3, b_1, b_3) are three imaginary axes perpendicular to each other, indicating the spatial relationships between the XCT images and the images (a_1, b_1).

The morphologies of the crack mouths in the CM and BJP specimens are illustrated in the Figs. 11(a) and (b), respectively. (In these images, the oxide products, which were present on the tested

specimens. were removed during image reconstruction, so as to clearly reveal the crack initiation sites.) Based on the marked location (yellow circles in Fig. 11(a)) of the crack mouth and the results in the corrosion section, it is inferred that the crack in the CM specimen initiated from boundaries such as the prior austenite and/or martensite lath boundaries, where NbC inclusions were found extensively. In comparison, in the BJP specimens, the crack originated from the pores that are present in the BJP specimen. It was found that six pores of various shapes and sizes served as the initiation sites as shown in Fig. 11(b) (The initiation sites were identified by coloring the crack blue. Consequently, the initiation sites in the figure appear blue and are circled with white dotted lines.). The cracks that initiated from them eventually coalesced into one large crack, as shown in Video 5.

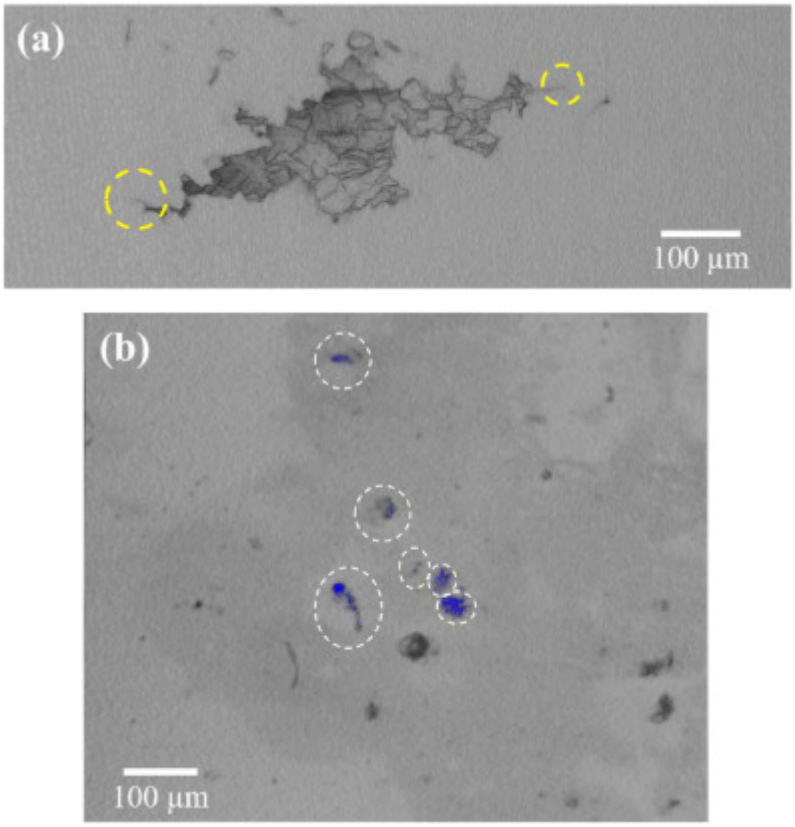

1. Download: Download high-res image (368KB)
2. Download: Download full-size image

Fig. 11. XCT images of the crack mouth in the (a) CM and (b) BJP specimens. The locations marked by white dotted curves in (b) are pores that acted as crack initiation sites. Note that blue coloring in (b) was used to highlight the inner part of the crack, making the crack initiation sites more visible.

The microstructural analysis for the crack observed in the CM specimen, characterized by using EBSD, is shown in Fig. 12(a_1-a_3, b_1-b_5), which confirms that the crack preferentially propagated along the martensite lath and prior austenite grain boundaries. With regard to the BJP, the tested specimen was ground and polished until one cross-section, including the crack scanned using XCT, was exposed. EDS mapping was performed on this cross-section. Results displayed in Fig. 13 confirm that the skeleton-like features shown in Fig. 10(b_3-b_6) and Video 4 indeed correspond to δ-ferrite. It is also apparent that the crack path was altered upon encountering this phase, Fig. 13(c_1, c_2)). Notably, the δ-ferrite did not dissolve upon getting exposed to the corrosive media (upon the dissolution of the surrounding matrix), suggesting a higher corrosion resistance of it compared to the martensite. Fracture surface analysis shown in Fig. 14 further supports the finding that the crack in the CM

specimen propagated preferentially along the martensite lath and prior austenite grain boundaries, with several facets of similar length to the martensite lath/prior austenite grain size.

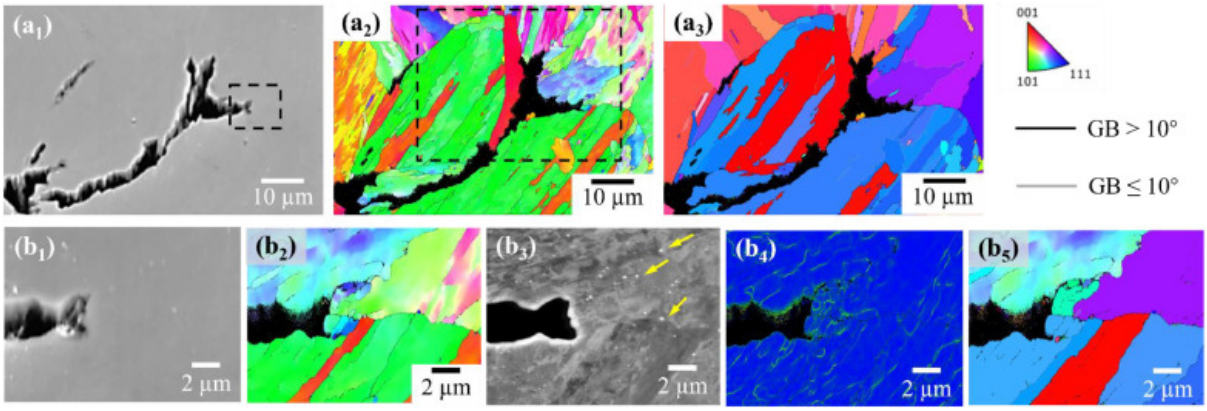

1. Download: Download high-res image (941KB)
2. Download: Download full-size image

Fig. 12. Crack tip and crack propagation path analysis in the CM specimen: a crack (a_1) and its IPF map (a_2) in a CM specimen; the reconstructed prior austenite map (a_3) of the same area as in (a_1, a_2); the SE image (b_1), IPF map (b_2), BSE image (b_3), KAM image (b_4), and reconstructed austenite map (b_5) of the crack tip area (black dotted rectangle in (a_1)). The yellow arrows in (b_3) indicate three examples of NbC inclusions.

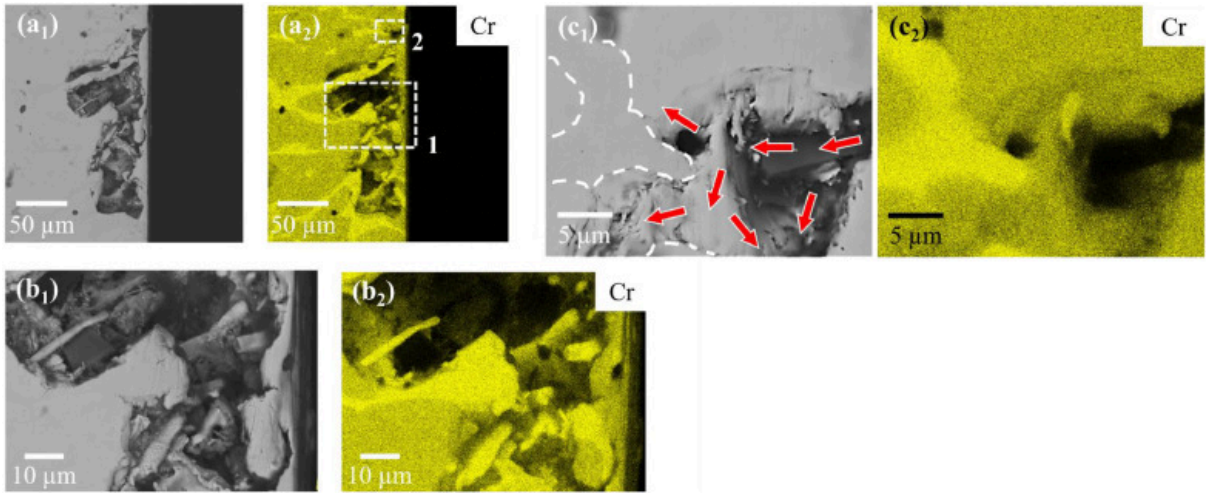

1. Download: Download high-res image (1MB)
2. Download: Download full-size image

Fig. 13. Crack propagation path analyses in the BJP specimen: a crack (a_1) and its EDS map for Cr element (a_2) in a BJP specimen; enlarged SEM image (b_1) and EDS map (b_2) of the white dotted rectangle 1 in (a_2); enlarged SEM image (c_1) and EDS map (c_2) of the white dotted rectangle 2 in (a_2). The δ-ferrite is marked by a white dotted line in (c_1), and the crack propagation path is indicated by red arrows in (c_1).

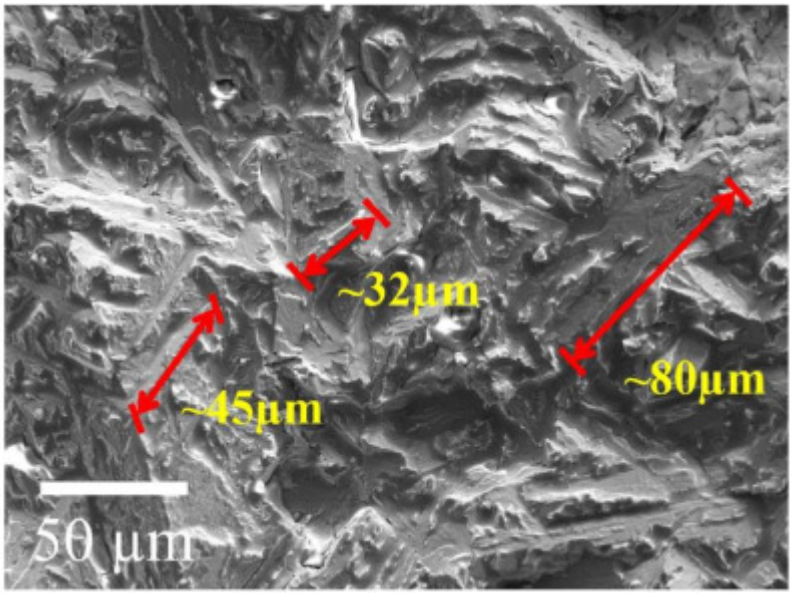

1. Download: Download high-res image (534KB)
2. Download: Download full-size image

Fig. 14. A fractographic image of the SCC tested CM specimen (90% YS SCC test, failed in 37 days).

4. Discussion

4.1. Microstructures

The microstructure of the CM specimens is predominantly martensite. During the solidification process of the 17-4 PH steel, body-centered cubic (bcc) δ-ferrite forms initially, which partially transforms into face-centered cubic (fcc) austenite via a peritectic reaction. Further cooling below the martensitic start temperature (M_s) results in the transformation of austenite into martensite through a displacive reaction. The c/a ratio of the martensite in 17-4 PH steel remains approximately one, attributed to the low carbon content (less than 0.07 wt.%) in it. The final microstructure is primarily body-centered cubic (bcc) martensite at room temperature, though retained austenite can also be present, depending on the cooling rate and M_s [26].

The processing steps involved in fabricating the BJP specimens induce δ-ferrite within the 17-4 PH steel, as illustrated in the Fig. 2(b_1-b_2). It is well known that the nucleation and growth of δ-ferrite in 17-4 PH occur when it is subjected to temperatures exceeding 1200 °C for prolonged durations and some of the δ-ferrite can be retained even after the material is cooled to room temperature [4,26,49]. Given that the sintering temperature of the BJP specimens examined in the present study was 1370 °C, a larger δ-ferrite content in them is expected [26]. The nucleation of δ-ferrite commences around ~1200 °C at the boundaries of austenitic grains, adhering to the Kurdjumov-Sachs orientation relationship. The formation of δ-ferrite embryos facilitates subsequent growth, aided by the ease of diffusion through the BCC phase, characterized by its relatively lower atomic packing fraction (compared to that of the austenite with the face centered cubic crystal structure) [50]. This mechanism helps rationalize the skeletal morphology of δ-ferrite, observed in their microstructures suggesting early nucleation followed by extensive growth periods.

HIP of the BJP specimens significantly modifies the microstructure. At the HIP temperature of 1160 °C, γ-austenite is a more thermodynamically stable phase, based on the ratio of Cr_{eq} to Ni_{eq} in 17–4 PH [51]. Hence, during the 4-hour HIP process, some of the δ-ferrite that is present in the as-sintered alloy transforms into γ-austenite. Thus, only 5.5 vol% of δ-ferrite is retained upon HIP and cooling to room

temperature. The applied pressure of 104 MPa during HIP is sufficient to induce recrystallization of the austenite matrix at this temperature, leading to a significant reduction in the austenite grain size [10]. While the MnS inclusions, which can act as sites for pitting corrosion in stainless steels [32,33], could not be observed in the CM specimen, relatively coarse ones were identified in both the BJP and HIP specimens, albeit in limited numbers. The growth of the MnS inclusions during heat treatment is governed by elemental diffusion. The Ostwald ripening theory [[52], [53], [54], [55]] provides an explanation for the size changes in nanoparticles, influenced by elemental diffusion and heat. According to this theory, the size of the MnS inclusions after heat treatment is determined by the initial size of the inclusions, the heat treatment temperature and time, and the diffusion coefficient of S, assuming other related factors like the equilibrium S concentration are the same or similar. As already mentioned, the BJP and HIP specimens were sintered at 1370 °C for 2 hours before proceeding with the solution heat treatment and aging process, unlike the CM specimens (the solution heat treatment and the following aging process were the same for all three types of specimens). Accordingly, at the onset of the solution heat treatment, the MnS inclusions in BJP and HIP specimens are likely to have a larger initial size compared to those in the CM specimens. This possibly led to the coarsening of the MnS inclusions in the BJP and HIP specimens. The HIP process could further increase the size of MnS inclusions due to prolonged exposure to elevated temperatures for an additional 4 hours. However, this anticipated further coarsening of MnS inclusions in the HIP specimens was not observed, suggesting that the MnS inclusions reached a saturated size, likely due to the exhaustion of the sulphur content (less than 0.03 wt.%) in the alloy.

In contrast to MnS, the NbC inclusions were not detected in the BJP and HIP specimens, whereas they were extensively present in the CM specimens. Previous studies have indicated that such inclusions begin to form at ~470 °C and completely decompose by ~1280 °C [41]. Since sintering of the BJP specimens was conducted at a temperature (1370 °C) that is much higher than the NbC's decomposition temperature, it is highly likely that any NbC or its nuclei were entirely decomposed during sintering, making the possibility of coarsening during subsequent heat treatments moot. This results in the absence of NbC in the as-sintered and HIP BJP samples. (While the possibility of NbC formation during the cooling phase of the sintering process exists, it can be ruled out as the specimens were not held at temperatures within the NbC formation range for any extended period during cooling.) In contrast, the temperatures used for hot rolling, solution heat treatment, and aging of the CM specimens are all above the NbC formation threshold but below 1280 °C, causing the inclusions to coarsen through these successive operations. The NbC precipitates, known to possess an fcc structure (space group Fm-3m, with a lattice parameter of 4.4 Å), exhibit either $M_{23}C_6$ or M_7C_3 stoichiometry and contribute to the hardening of MSSs [[56], [57], [58]]. Prior studies [40,59,60] have shown that NbC is primarily located at the prior austenite grain and martensite lath boundaries, but they can also be present inside the martensite laths.

4.2. Corrosion properties

From the results of the corrosion tests, it is clear that, among the three types of specimens studied, the BJP specimens exhibit the lowest corrosion resistance, as measured by the corrosion rate. Results of the immersion and GL tests, as shown in Figs. 7(b_1-b_3) and 8(b_1-b_4), indicate that the pores in the BJP specimens were preferentially attacked during these tests. Notably, in the GL tests, where a large current density was applied, two pores were observed to connect with each other. This suggests that the corrosion of pores could result in their coalescence when the extent of corrosion is significant. Several studies have acknowledged that porosity that is inherent to powder-based AM technologies

can deteriorate the corrosion properties of stainless steels (and other alloys) and serve as initiation sites for pitting [1,12,19,40,[61], [62], [63]]. The mechanism behind this phenomenon is well established [13,64,65]. It has been reported that oxygen is rapidly depleted inside the pores, leading to an oxygen-depleted environment compared to the bulk solution. This condition reduces the potential at the bottom of the pores compared to the mouth of the pores or the external surface. Consequently, the external areas act as the cathodic sites, accompanied by severe anodic activity inside the pore, which leads to the initiation of corrosion. The anodic reactions produce metal cations that attract deleterious anions such as Cl^- into the pores, hindering re-passivation and, in the process, further exacerbate corrosion. Moreover, the reaction of metal ions with hydroxyl ions alters the electrolyte chemistry inside the pores towards a lower pH. This change in chemistry deactivates and impedes the formation of the passive layer. The detrimental effects of electrolyte chemistry changes inside the pores on the passive films are illustrated by the results displayed in the Fig. 9(a) and listed in Table 2, which shows that the BJP specimens requires a significantly higher passive current density compared to the other specimens. Furthermore, the BJP specimens exhibit a lower breakdown/pitting potential, suggesting that their passive films overall are less stable than those on the CM and HIP specimens. This supports the assertion that the alterations in the electrolyte chemistry within the pores hinder and weaken the formation of the passive layer inside the pores. The EIS results shown in the Fig. 9(b_1, c) and Table 3 further reveal that the oxide films on BJP specimens are less protective compared to those on the CM and HIP specimens. Notably, a significantly lower R_{CT} of the BJP specimens suggests a much easier charge transfer process, which is due to the de-passivation of oxide films within the pores as previously mentioned.

Furthermore, the 3D nature of the pores increases the effective surface area available for corrosion reactions and thereby increasing the corrosion rate. A larger Y_0 of the CPE1 noted for the BJP specimens was also caused by the increased area. While pores of all diameters expedite corrosion attacks, smaller pores (<10 μm) can still support the formation of a passive film, thereby reducing, but not eliminating, the risk of localized corrosion [66,67]. The distribution of pore sizes in the BJP specimens, as detailed in [10] (refer to the data displayed for "batch A" in Fig. S1 in the supplementary document), clearly shows that the majority of pores possess a square root area larger than 10 μm (the largest square root area found was ~315 μm). Given the significantly higher porosity and large pore size in the BJP specimens, it is logical that they exhibit the highest corrosion rate and the lowest corrosion potential among the three types of specimens examined in this work.

Considering the role of porosity on the corrosion resistance (discussed above), it is not surprising to see that the HIP specimens exhibit a far superior corrosion resistance, measured by the corrosion rate, as illustrated in Fig. 9(a) and Table 2. The HIP process significantly reduced both the number and the size of pores inherited from the BJP process. After HIP, the square root area of the largest pores decreased from ~315 to ~25 μm, and more than half of the pores had a square root area of less than 10 μm [10] (refer to the data for "batch A+HIP" in Fig. S1 in the supplementary document). However, the porosity in the HIP specimens still higher than that in the CM specimens (which contain zero porosity by virtue of the fact that they were hot rolled that would close any residual porosity from casting). Therefore, the reduction in their corrosion rate may not be solely attributed to the decrease in pore number and size. It is important to note that the CM specimen contained a significantly higher amount of NbC compared to the HIP specimens. Clark et al. [68] emphasized the nobility of the NbC phase, suggesting its cathodic behaviour relative to the matrix, which could potentially initiate localized corrosion of adjacent areas through galvanic corrosion. This inclusion also disrupts the

continuity of the oxide film, thereby degrading its quality, leading to the higher corrosion rate of the CM specimens compared to the HIP specimens.

In addition, the HIP specimens contain a relatively higher δ-ferrite fraction after the HIP process, compared to the CM specimens. Many studies have indicated that the corrosion rate of ferrite is significantly slower, by approximately 2 to 3 times, compared to that of the martensite [69]. On the other hand, Fushimia et al. reported that in dual-phase steel, galvanic corrosion, which arises from the galvanic cell between ferrite and martensite, can lead to lower corrosion resistance [70]. Our findings, illustrated in the Fig. 6, show that δ-ferrite exhibits a higher Volta potential (directly related to EWF) than surrounding martensite, leading to the formation of galvanic cells between δ-ferrite and martensite when immersed in a corrosive solution. Initially, this accelerates martensite corrosion, particularly at the δ-ferrite/martensite interface [46]. However, the subsequent formation of the oxide films mitigates this effect [46]. Once the oxide films have formed on both the phases, the galvanic corrosion between them becomes unsustainable. Consequently, the inherently slower corrosion rate of δ-ferrite predominates after the cessation of galvanic interactions between the phases [46]. The presence of δ-ferrite in the HIP specimens, due to its slower corrosion rate, results in a smaller area that is prone to high corrosion rate compared to the CM specimens, contributing to the HIP specimens' lower overall corrosion rate. The EIS results further reveal that oxide films on HIP specimens offer superior protection compared to those on other specimens. To summarize, the enhanced protective quality of the oxide films on the HIP specimens is possibly due to the combined effects of the following: (i) absence of NbC inclusions, (ii) reduced pore size and number, and (iii) the high Cr concentration in δ-ferrite. The first two of these are already discussed. Coming to the third, according to the Fick's law, the elevated Cr concentration facilitates the diffusion of Cr into the oxide films, thus enriching the Cr content in them, and, in turn, enhances their protectiveness [71]. A higher Cr content in the oxide film on the δ-ferrite was confirmed through the STEM-EDS analysis shown in Fig. 15. Therefore, the HIP specimens, characterized by a higher δ-ferrite fraction, have a larger surface area covered by more protective oxide films compared to the CM specimens, leading to their lower overall corrosion rate.

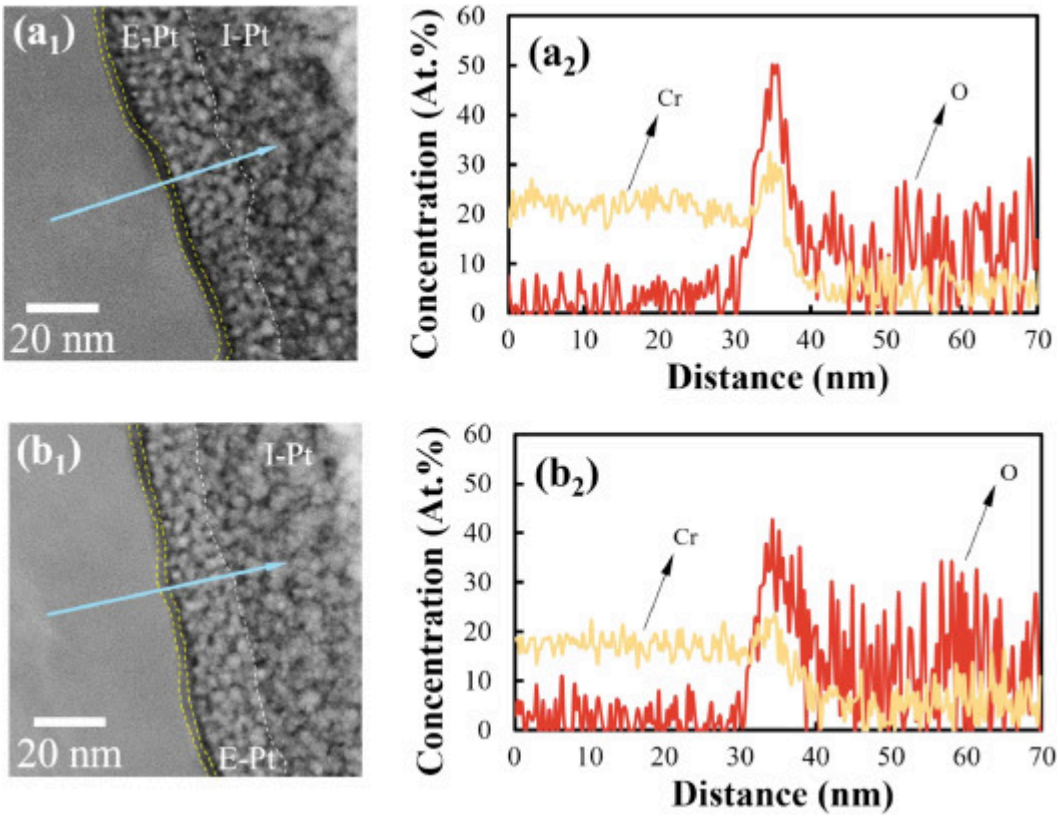

1. Download: Download high-res image (816KB)
2. Download: Download full-size image

Fig. 15. STEM analysis of oxide film on δ-ferrite (a_1) and martensite (b_1), with STEM EDS line scan results marked by the blue arrows in (a_1) and (b_1) shown in (a_2) and (b_2), respectively. E-Pt and I-Pt in (a_1, b_1) represent the Pt layer deposited by electron beam and ion beam, respectively.

The immersion test results of the HIP specimens, Fig. 7(c_1-c_2), indicate that the ferrite/martensite interface, and some locations inside the ferrite, underwent corrosion attacks. Compared to the non-corroded specimens, the corroded locations appear to correspond to the Cu-enriched particles. The STEM EDS results presented in Figs. 5 reveal that at the Cu-enriched locations in the ferrite or along the ferrite/martensite interfaces, Cr was depleted. It is well accepted that Cr plays a more crucial role than Cu in the formation of protective films [72]. Therefore, Cr depletion at these locations can degrade the oxide films formed on the corresponding area, leading to localized corrosion. Notably, Cu itself can form a galvanic cell with the surrounding Fe, when the oxide film is degraded, facilitating the corrosion of the surrounding matrix and forming holes similar to those shown in Fig. 7(c_1-c_2).

The GL results in Fig. 8(c_1-c_2) also showed corrosion attack along the ferrite/martensite interface, but with a more continuous attack compared to the immersion test results. This may be because the current density applied during the GL tests is much higher than the natural condition that prevail during the immersion tests, leading to a larger breakdown area of the passive film per unit time than in the immersion tests. Consequently, not only a greater Cu-enriched area would be exposed, but also more of the ferrite/martensite interface is available to the corrosive media to access. The formation of a galvanic cell between the ferrite and martensite interface leads to the corrosion of the interface, and a more continuous corrosion morphology.

The presence of the coarser MnS particles in the microstructures of the BJP and HIP specimens could also have contributed to the deterioration of their corrosion properties to some extent, as they serve

as the anodic sites during corrosion [1,19,29,31,33]. However, due to their comparatively small size (less than 10 μm), the resultant pits from their dissolution are likely to be less detrimental. This hypothesis is supported by the results of the SCC tests, which will be discussed later, where the cracks in the BJP specimens were observed to initiate from pores, while no observable crack could be detected in the HIP specimen.

The cyclic potentiodynamic polarization test results, Fig. 9 (a), revealed that the HIP specimens exhibited a lower breakdown/pitting potential compared to the CM specimens. Breakdown/pitting potential is defined as the potential at which there is a rapid increase in current density during anodic polarization, occurring before reaching the oxygen evolution potential [73]. This surge in current density results from the passive film's breakdown or its breakdown followed by material pitting [73]. The lower breakdown/pitting potential in the HIP specimens is attributed to the martensite's increased susceptibility to pitting upon the breakdown of the oxide film. Specifically, when the oxide film breaks down, a galvanic cell between ferrite and martensite re-forms, accelerating the corrosion of the martensite and at the ferrite/martensite interface. Despite the fact that the EIS results suggesting less protective oxide films in CM specimens, the absence of significant galvanic cell formation means that, even upon oxide film breakdown, the increase in current density is delayed until a higher potential is reached, indicating a more challenging pitting initiation compared to that in the HIP specimens.

Another critical observation from the cyclic potentiodynamic curves is the notably smaller hysteresis loop in the HIP specimens compared to those of the CM and BJP specimens. A smaller loop suggests that fewer of the passive films formed on the HIP specimens underwent breakdown and that these films were more readily reformed [73]. This phenomenon can be attributed to the oxide films on δ-ferrite being more protective and less prone to breakdown than those on martensite. Furthermore, even if the δ-ferrite oxide films do break down, they are more quickly restored due to faster Cr diffusion, unlike the oxide films on martensite. With a higher δ-ferrite fraction compared to the CM specimens, the HIP specimens thereby showed a smaller hysteresis loop. As noted, pores can significantly impair the protective qualities of oxide films formed within them and obstruct their ability to re-passivate. However, despite the BJP specimens having a substantial number of large pores, their hysteresis loop size is comparable to that of the CM specimens. This suggests that the beneficial impact of δ-ferrite on the oxide films is also present in the BJP specimens, given the high δ-ferrite content in them. This effect partially mitigates the adverse consequences caused by the pores. However, it is worth noting that it does not completely neutralize them, as evidenced by the BJP specimens still exhibiting a higher corrosion rate compared to the CM specimens.

The results of the immersion and GL tests performed on the CM specimens revealed that areas near the NbC inclusions are particularly susceptible to corrosion attacks. This is attributed to the cathodic properties of the NbC inclusions, as previously discussed. A recent study [40] discovered that refining the NbC phase using laser beam melting AM technology improves the corrosion resistance of the 17-4 PH stainless steel subjected to H900 aging heat treatment, in comparison to the CM specimens. These findings support that NbC inclusions are detrimental to the corrosion resistance of the material, which is consistent with the observations of the present study. A comparative study performed by Stoudt et al. [74] on the corrosion properties of CM and LPBF 17-4 PH also demonstrated that the pitting potential of the latter steel exceeded that of its CM counterpart. This improvement was attributed to the finer NbC inclusions generated by the LPBF process, further underscoring the adverse influence of NbC inclusions on localized corrosion. However, in the current study, no similar improvement in pitting potential was observed in the BJP and HIP specimens, despite the BJP process

resulting in a NbC inclusion free alloy (at least within the resolution of the microstructural characterization performed in the present study). This result again indicates that the intrinsic porosity associated with the BJP technique detrimentally affects the localized corrosion resistance of the material. The NbC inclusions are also a contributing factor to the degradation of the oxide films formed on the CM specimens (Fig. 9(b_1, c) and Table 3) and increased the corrosion rate of the CM specimens compared to the HIP specimens (Table 2).

4.3. SCC resistance

Results of the SCC tests indicate that the CM specimens have a considerably lower SCC resistance when compared to the BJP and HIP specimens, which is surprising given that the presence of pores within the BJP alloy significantly diminishes its corrosion resistance. The mechanistic origins for this are discussed in the following.

From the Fig. 11(b) and Video 5, it is evident that the cracks in the BJP specimens originated from the pores. Unlike the initiation sites in the CM specimens, which were shown to be severely corroded/cracked, the pore mouths in the BJP specimens did not exhibit significant corrosion. This observation suggests that the cracks initiated from within the pores, corroborating the earlier assertion that changes in electrolyte chemistry trigger the de-passivation of the oxide films formed within them, and cause severe anodic reactions inside the pores. As discussed, six pores acted as the corrosion initiation sites, and the cracks that initiated from them appear to eventually coalesce into one large crack, as shown in Video 5. This result is consistent with the GL test results, which suggest that when the amount of corrosion is significant, pores tend to connect with each other. A recent study by Burns et al. [75] also demonstrated that sub-micrometer porosity contributed to the enhancement of environmentally assisted cracking in LPBF 17-4 PH, although the specific role of porosity in crack initiation was not thoroughly examined in that investigation.

The interiors of a crack in the BJP specimen, Fig. 10(b_3-b_6), and video 4, reveal brighter skeletal features resembling δ-ferrite, which remains undissolved during the SCC test. EDS mapping of the cross-section containing the crack in Fig. 13 confirmed that these features are indeed δ-ferrite. These findings indicate that δ-ferrite is more corrosion-resistant than martensite. Results from the corrosion tests in the previous section also suggest that the δ-ferrite has beneficial effects on the corrosion properties of this material. To illustrate the extensive distribution of δ-ferrite inside the crack shown in Fig. 10(b_1), a 3D reconstruction of the non-dissolved δ-ferrite was performed and is presented in Video 6. A section of the 3D reconstruction is shown in Fig. S4 (supplementary document). The δ-ferrite in the video and the figure is rendered in green. This reconstruction is based on the brightness of the XCT images, so the green part represents the estimated morphology of the δ-ferrite. From the figure and the video, it can be observed that the δ-ferrite, which acts as a barrier to crack propagation, was extensively present.

All the observations from both the corrosion tests and SCC tests reinforce the previous assertion that δ-ferrite positively influences the material's corrosion-related properties. From the images displayed in Fig. 13, it is observed that the crack initially propagated in a direction perpendicular to the loading direction. However, upon encountering δ-ferrite, it was unable to penetrate this corrosion-resistant phase. Instead, the crack circumvents the δ-ferrite, resulting in a blunted crack morphology whose length runs parallel to the loading direction. In effect, the δ-ferrite phases within the microstructure act as uncracked ligaments and bridge the crack faces. Such bridging lowers the crack driving force and hence, requires the application of additional load for further propagation of it [76]. This phenomenon, referred to as deflection-induced toughening, mirrors mechanisms observed in

biological structures, such as bones with osteonal structures [76]. Furthermore, the deflection of the crack reduces the effective driving force for its propagation compared to a straight crack of the same length, thereby enhancing the material's resistance to SCC [77].

As already mentioned, it is inferred that the crack during SCC initiate from boundary-like features in the CM specimens. Prior studies [40,59,60] have shown that the NbC inclusions are mainly located along the prior austenite boundaries and the martensite lath boundaries, although some inclusions were also noted inside the martensite laths. Based on the corrosion results, it is considered that these inclusions made the boundaries more vulnerable and made them the crack initiation locations.

The crack observed in the CM specimen, Fig. 10(a_3-a_6) and Video 2, is more straight compared to that in the BJP specimen, due to the fewer barriers, such as δ-ferrite, for its growth. As a result, it grows primarily in the direction perpendicular to the loading direction, which is also the surface with maximum normal stress. These indicate a larger effective driving force for propagation in the CM specimen [77], leading to the shorter SCC failure time, compared to the BJP specimens. Crack tip analysis, as indicated in the figure, suggests that the crack tends to propagate along the martensite lath and prior austenite grain boundaries. This propagation pattern should also be attributed to the distribution of NbC inclusions along these boundaries, for reasons previously mentioned. Such a distribution is clearly visible in the BSE image in Fig. 12(b_3). The brighter spots in the BSE image correspond to the NbC inclusions (confirmed with EDS analysis). From this image and other related images in Fig. 12, it is evident that these inclusions are primarily located on the boundaries, with those along the boundaries generally being larger than those observed inside the martensite laths. Notably, several large NbC inclusions were detected along the boundaries along which the crack has propagated. Additionally, the KAM map in Fig. 12(b_4) of the crack tip area shows that localized deformation occurs mainly along the aforementioned boundaries. Such localized deformation will increase strain energy locally, which, in turn, facilitate easier corrosion. This, in turn, contributes to the tendency of crack tip growth along these boundaries.

In the HIP specimens, XCT did not reveal any cracks. The results of the corrosion tests indicate that corrosion should have occurred at sites like MnS inclusions and the ferrite/martensite interfaces. However, (a) due to the limited number and smaller size of the MnS inclusions and (b) the fact that once the oxide film has formed, the galvanic cell between the martensite and ferrite cannot be sustained, the corrosion that occurred is possibly insufficient to lead to cracking. Unlike the CM specimens, which possess a significant number of NbC inclusions along boundaries, the HIP specimens did not have such corrosion susceptible locations either. All these factors—in combination—probably contributed to crack suppression during the SCC tests of the HIP specimens.

Schematic illustrations that summarize the understanding developed in this study on the corrosion/crack initiation, and propagation mechanisms in different 17-4 PH specimens examined are shown in Fig. 16. In the CM specimens, corrosion initiates at the NbC inclusions and then progresses along boundaries such as prior austenite/martensite lath boundaries. This leads to the development of sharp cracks, which propagate along these boundaries and generally perpendicular to the loading direction. In the BJP specimens, corrosion originates within the numerous pores and then forms cracks. Upon encountering the δ-ferrite phase present in the microstructure, the cracks are bridged and blunted, and do not primarily propagate perpendicular to the loading direction. In the HIP specimens, although corrosion occurs at the ferrite/martensite interfaces and the MnS inclusions, it does not lead to observable cracks due to the limited size and quantity of these inclusions and the unsustainable galvanic cell between δ-ferrite and martensite.

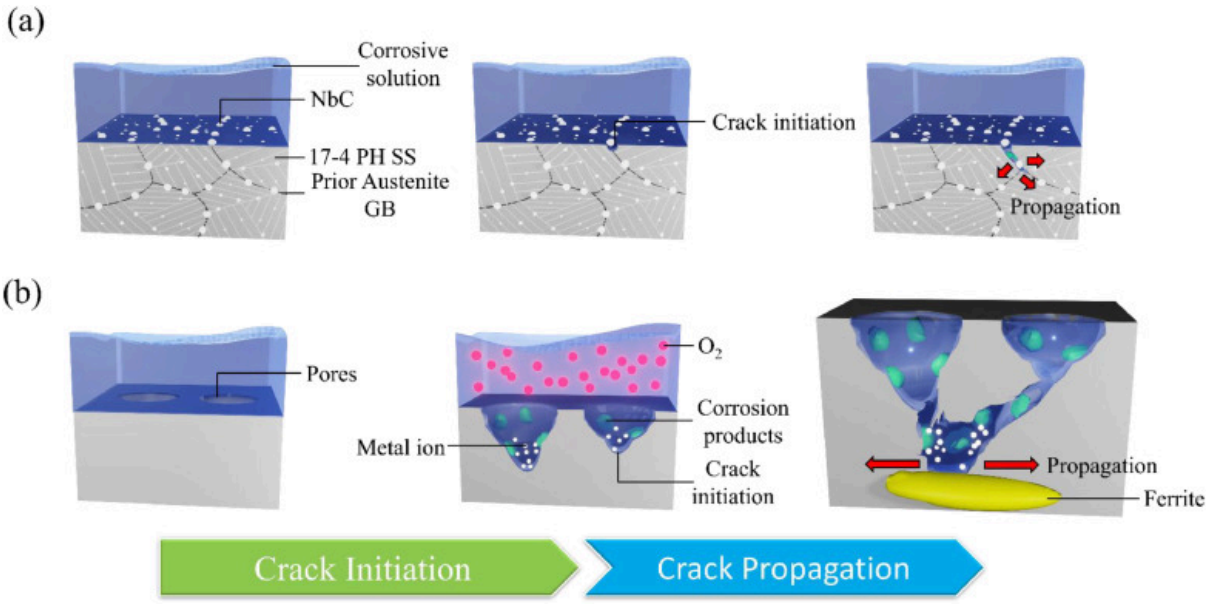

1. Download: Download high-res image (582KB)
2. Download: Download full-size image

Fig. 16. Schematic of corrosion and crack initiation and propagation behaviors in the (a) CM and (b) BJP specimens.

5. Summary, conclusions, and implications

A comprehensive experimental study on the corrosion and stress corrosion cracking resistances of the 17-4 PH martensitic stainless steel that was additively manufactured using the binder jet printing technology was conducted. Results obtained on the as-sintered BJP specimens, with relatively higher porosity content, and those subjected to the HIP treatment, for reducing the porosity, were compared with those obtained on the CM specimens that have no porosity. In addition to the porosity variations, the microstructural constituents in the three types of 17-4 examined also vary: while the BJP and HIP specimens contain δ-ferrite and MnS inclusions, the CM ones do not contain either of them, but have NbC inclusions. Together, these affect the studied properties in diverse ways. The following are the two key conclusions that can be drawn from this work.

- (1) The NbC inclusions present in CM 17-4 PH adversely affected its corrosion and SCC resistances, while the porosity that exists the BJP specimens degraded their corrosion performance. However, the δ-ferrite phase, which results from the sintering process employed for producing the BJP specimens, imparts superior SCC resistance to them.
- (2) The HIP process, performed after sintering of the BJP specimens, reduces both the porosity and δ-ferrite content, which, collectively, lead to enhanced corrosion and SCC resistances that are superior to those of CM 17-4 PH.

Before closing, it is worth highlighting the implications of the present work's results in the broader context of the AM alloys. In literature, alloys that are produced using different AM techniques are often ‘banded’ together and given a general treatment. However, their microstructural features can be vastly different; even the same alloy that was produced using two different AM methods can have distinct microstructural attributes, which can result in significantly different mechanical and functional behaviours. In the context of BJP, the efforts that were made hitherto for understanding the processing-microstructure-properties are relatively meagre, despite its increasing prominence as an attractive AM technique for producing parts economically and in volume. This is because of the

notion—albeit not an accurate one—that the overall microstructural similarity between the BJP and CM alloys renders a property similarity as well. While this may be true—to some extent and especially in the context of quasi-static tensile properties (for example), subtle microstructural differences can lead to substantial divergences in properties that are critical for ensuring structural integrity and reliability (such as unnotched fatigue and SCC), as this and some prior studies [34] unequivocally demonstrate. The porosity present in the alloys adds an additional degree of complexity, which might not be detrimental in all contexts. While HIP is often considered as a panacea for all the porosity-induced problems, it might not be needed in specific contexts, as HIP can coarsen the microstructure and, thus, result in degradation of some properties (such as the yield strength). Therefore, it becomes imperative to evaluate the processing-microstructure-porosity-performance relationships critically for each alloy, before components produced using the AM techniques are widely deployed.

CRediT authorship contribution statement

Yida Xiong: Writing – original draft, Investigation. **Jayaraj Radhakrishnan:** Writing – review & editing, Investigation. **Sheng Huang:** Writing – review & editing, Methodology, Investigation. **Yusheng Chua:** Investigation. **Wei Shi:** Writing – review & editing. **Upadrasta Ramamurty:** Writing – review & editing, Supervision, Resources, Project administration, Funding acquisition, Conceptualization.

Declaration of competing interest

The authors declare that they have no known competing financial interests or personal relationships that could have appeared to influence the work reported in this paper.

Acknowledgements

Financial support from the Agency for Science, Technology and Research (A*STAR) of Singapore via the Structural Metal Alloys Programme (No. A18B1b0061) is gratefully acknowledged. We thank Dr. Jim McKinnell and Ms. Alexis Bryl of HP Inc., Corvalis, USA for providing us with the BJP 17-4 PH samples tested in this study, and Prof. Daniel Blackwood and Dr. Kai Xiang Kuah of the National University of Singapore for their assistance with electrochemical experiments.

Appendix. Supplementary materials

Download all supplementary files included with this article

What's this?

Download: Download Powerpoint document (424MB)Download: Download Word document (3MB)

References

1. [1]

A. Hemmasian Ettefagh, S. Guo, J. Raush

Corrosion performance of additively manufactured stainless steel parts: a review

Addit. Manuf., 37 (2021), Article 101689, 10.1016/j.addma.2020.101689

View PDFView articleView in ScopusGoogle Scholar

2. [2]

A. Mostafaei, R. Ghiaasiaan, I.-T. Ho, S. Strayer, K.-C. Chang, N. Shamsaei, S. Shao, S. Paul, A.-C. Yeh, S. Tin, A.C. To

Additive manufacturing of nickel-based superalloys: a state-of-the-art review on process-structure-defect-property relationship

Prog. Mater. Sci., 136 (2023), Article 101108, 10.1016/j.pmatsci.2023.101108

View PDFView articleView in ScopusGoogle Scholar

3. [3]

S. Sabooni, A. Chabok, S.C. Feng, H. Blaauw, T.C. Pijper, H.J. Yang, Y.T. Pei

Laser powder bed fusion of 17–4 PH stainless steel: a comparative study on the effect of heat treatment on the microstructure evolution and mechanical properties
Addit. Manuf., 46 (2021), Article 102176, 10.1016/j.addma.2021.102176
View PDFView articleView in ScopusGoogle Scholar

4. [4]

D. Huber, L. Vogel, A. Fischer
The effects of sintering temperature and hold time on densification, mechanical properties and microstructural characteristics of binder jet 3D printed 17-4 PH stainless steel
Addit. Manuf., 46 (2021), Article 102114, 10.1016/j.addma.2021.102114
View PDFView articleView in ScopusGoogle Scholar

5. [5]

C. Zheng, A. Mostafaei, P.R. De Vecchis, I. Nettleship, M. Chmielus
Microstructure evolution for isothermal sintering of binder jet 3D printed alloy 625 above and below the solidus temperature
Addit. Manuf., 47 (2021), Article 102276, 10.1016/j.addma.2021.102276
View PDFView articleView in ScopusGoogle Scholar

6. [6]

T.H. Becker, P. Kumar, U. Ramamurty
Fracture and fatigue in additively manufactured metals
Acta Mater, 219 (2021), Article 117240, 10.1016/j.actamat.2021.117240
View PDFView articleView in ScopusGoogle Scholar

7. [7]

A. Mostafaei, P. Rodriguez De Vecchis, I. Nettleship, M. Chmielus
Effect of powder size distribution on densification and microstructural evolution of binder-jet 3D-printed alloy 625
Mater. Des., 162 (2019), pp. 375-383, 10.1016/j.matdes.2018.11.051
View PDFView articleView in ScopusGoogle Scholar

8. [8]

P. Nandwana, A.M. Elliott, D. Siddel, A. Merriman, W.H. Peter, S.S. Babu
Powder bed binder jet 3D printing of Inconel 718: densification, microstructural evolution and challenges☆
Curr. Opin. Solid State Mater. Sci., 21 (2017), pp. 207-218, 10.1016/j.cossms.2016.12.002
View PDFView articleView in ScopusGoogle Scholar

9. [9]

H. Miyanaji, K.M. Rahman, M. Da, C.B. Williams
Effect of fine powder particles on quality of binder jetting parts
Addit. Manuf., 36 (2020), Article 101587, 10.1016/j.addma.2020.101587
View PDFView articleView in ScopusGoogle Scholar

10. [10]

J. Radhakrishnan, P. Kumar, S.S. Gan, A. Bryl, J. McKinnell, U. Ramamurty
Microstructure and tensile properties of binder jet printed 17–4 precipitation hardened martensitic stainless steel
Mater. Sci. Eng. A, 860 (2022), Article 144270, 10.1016/j.msea.2022.144270
View PDFView articleView in ScopusGoogle Scholar

11. [11]
J. Radhakrishnan, P. Kumar, S.S. Gan, A. Bryl, J. McKinnell, U. Ramamurty
Fatigue resistance of the binder jet printed 17-4 precipitation hardened martensitic stainless steel
Mater. Sci. Eng. A, 865 (2023), Article 144451, 10.1016/j.msea.2022.144451
View PDFView articleView in ScopusGoogle Scholar
12. [12]
R.F. Schaller, J.M. Taylor, J. Rodelas, E.J. Schindelholz
Corrosion properties of powder bed fusion additively manufactured 17-4 PH stainless steel
CORROSION, 73 (2017), pp. 796-807, 10.5006/2365
View in ScopusGoogle Scholar
13. [13]
K. Geenen, A. Röttger, W. Theisen
Corrosion behavior of 316L austenitic steel processed by selective laser melting, hot-isostatic pressing, and casting
Mater. Corros., 68 (2017), pp. 764-775, 10.1002/maco.201609210
View in ScopusGoogle Scholar
14. [14]
M. Laleh, A.E. Hughes, W. Xu, I. Gibson, M.Y. Tan
Unexpected erosion-corrosion behaviour of 316L stainless steel produced by selective laser melting
Corros. Sci., 155 (2019), pp. 67-74, 10.1016/j.corsci.2019.04.028
View PDFView articleView in ScopusGoogle Scholar
15. [15]
M. Ziętala, T. Durejko, M. Polański, I. Kunce, T. Płociński, W. Zieliński, M. Łazińska, W. Stępniowski, T. Czujko, K.J. Kurzydłowski, Z. Bojar
The microstructure, mechanical properties and corrosion resistance of 316L stainless steel fabricated using laser engineered net shaping
Mater. Sci. Eng. A, 677 (2016), pp. 1-10, 10.1016/j.msea.2016.09.028
View PDFView articleView in ScopusGoogle Scholar
16. [16]
M. Laleh, A.E. Hughes, S. Yang, J. Li, W. Xu, I. Gibson, M.Y. Tan
Two and three-dimensional characterisation of localised corrosion affected by lack-of-fusion pores in 316L stainless steel produced by selective laser melting
Corros. Sci., 165 (2020), Article 108394, 10.1016/j.corsci.2019.108394
View PDFView articleView in ScopusGoogle Scholar
17. [17]
R.F. Schaller, A. Mishra, J.M. Rodelas, J.M. Taylor, E.J. Schindelholz
The role of microstructure and surface finish on the corrosion of selective laser melted 304L
J. Electrochem. Soc., 165 (2018), pp. C234-C242, 10.1149/2.0431805jes
View in ScopusGoogle Scholar
18. [18]
G. Ko, W. Kim, K. Kwon, T.-K. Lee
The corrosion of stainless steel made by additive manufacturing: a review
Metals, 11 (2021), p. 516, 10.3390/met11030516
Google Scholar

19. [19]
M. Alnajjar, F. Christien, V. Barnier, C. Bosch, K. Wolski, A.D. Fortes, M. Telling
Influence of microstructure and manganese sulfides on corrosion resistance of selective laser melted 17-4 PH stainless steel in acidic chloride medium
Corros. Sci., 168 (2020), Article 108585, 10.1016/j.corsci.2020.108585
View PDFView articleView in ScopusGoogle Scholar
20. [20]
U.K. Viswanathan, S. Banerjee, R. Krishnan
Effects of aging on the microstructure of 17-4 PH stainless steel
Mater. Sci. Eng. A, 104 (1988), pp. 181-189, 10.1016/0025-5416(88)90420-X
View PDFView articleView in ScopusGoogle Scholar
21. [21]
M. Karaminezhaad, S. Sharafi, K. Dalili
Effect of molybdenum on SCC of 17-4PH stainless steel under different aging conditions in chloride solutions
J. Mater. Sci., 41 (2006), pp. 3329-3333, 10.1007/s10853-005-5416-8
View in ScopusGoogle Scholar
22. [22]
Y.H. Fan, H.L. Zhao, K.R. Weng, C. Ma, H.X. Yang, X.L. Dong, C.W. Guo, Y.G. Li
The role of delta ferrite in hydrogen embrittlement fracture of 17-4 PH stainless steel
Int. J. Hydrog. Energy, 47 (2022), pp. 33883-33890, 10.1016/j.ijhydene.2022.07.257
View PDFView articleView in ScopusGoogle Scholar
23. [23]
M. Alnajjar, F. Christien, C. Bosch, K. Wolski
A comparative study of microstructure and hydrogen embrittlement of selective laser melted and wrought 17–4 PH stainless steel
Mater. Sci. Eng. A, 785 (2020), Article 139363, 10.1016/j.msea.2020.139363
View PDFView articleView in ScopusGoogle Scholar
24. [24]
C.N. Hsiao, C.S. Chiou, J.R. Yang
Aging reactions in a 17-4 PH stainless steel
Mater. Chem. Phys., 74 (2002), pp. 134-142, 10.1016/S0254-0584(01)00460-6
View PDFView articleView in ScopusGoogle Scholar
25. [25]
W.D. Yoo, J.H. Lee, K.T. Youn, Y.M. Rhyim
Study on the microstructure and mechanical properties of 17-4 PH stainless steel depending on heat treatment and aging time
Solid State Phenom, 118 (2006), pp. 15-20, 10.4028/www.scientific.net/SSP.118.15
Google Scholar
26. [26]
A.S. Murthy, Role of alloy additions on strengthening in 17-4 PH stainless steel, (n.d.).
Google Scholar
27. [27]
D. Carrouge, H.K.D.H. Bhadeshia, P. Woollin

Effect of δ -ferrite on impact properties of supermartensitic stainless steel heat affected zones
Sci. Technol. Weld. Join., 9 (2004), pp. 377-389, 10.1179/136217104225021823
View in ScopusGoogle Scholar

28. [28]
P. Wang, S.P. Lu, N.M. Xiao, D.Z. Li, Y.Y. Li
Effect of delta ferrite on impact properties of low carbon 13Cr–4Ni martensitic stainless steel
Mater. Sci. Eng. A, 527 (2010), pp. 3210-3216, 10.1016/j.msea.2010.01.085
View PDFView articleView in ScopusGoogle Scholar

29. [29]
Z. Duan, C. Man, H. Cui, Z. Cui, X. Wang
Formation mechanism of MnS inclusion during heat treatments and its influence on the pitting behavior of 316L stainless steel fabricated by laser powder bed fusion
Corros. Commun., 7 (2022), pp. 12-22, 10.1016/j.corcom.2022.04.002
View PDFView articleView in ScopusGoogle Scholar

30. [30]
U. Kamachi Mudali, A.K. Bhaduri, J.B. Gnanamoorthy
Localised corrosion behaviour of 17–4 PH stainless steel
Mater. Sci. Technol., 6 (1990), pp. 475-481, 10.1179/mst.1990.6.5.475
Google Scholar

31. [31]
D. Li, F. Huang, X. Lei, Y. Jin
Localized corrosion of 304 stainless steel triggered by embedded MnS
Corros. Sci., 211 (2023), Article 110860, 10.1016/j.corsci.2022.110860
View PDFView articleView in ScopusGoogle Scholar

32. [32]
Z. Duan, C. Man, C. Dong, Z. Cui, D. Kong, L. Wang, X. Wang
Pitting behavior of SLM 316L stainless steel exposed to chloride environments with different aggressiveness: pitting mechanism induced by gas pores
Corros. Sci., 167 (2020), Article 108520, 10.1016/j.corsci.2020.108520
View PDFView articleView in ScopusGoogle Scholar

33. [33]
D. Nakhaie, M.H. Moayed
Pitting corrosion of cold rolled solution treated 17-4 PH stainless steel
Corros. Sci., 80 (2014), pp. 290-298, 10.1016/j.corsci.2013.11.039
View PDFView articleView in ScopusGoogle Scholar

34. [34]
P. Kumar, R. Jayaraj, J. Suryawanshi, U.R. Satwik, J. McKinnell, U. Ramamurty
Fatigue strength of additively manufactured 316L austenitic stainless steel
Acta Mater, 199 (2020), pp. 225-239, 10.1016/j.actamat.2020.08.033
View PDFView articleGoogle Scholar

35. [35]
ASTM G39-99: standard practice for preparation and use of bent-beam stress-corrosion test specimens, (n.d.).
Google Scholar

36. [36]
AMS2759/3J: heat treatment, precipitation-hardening corrosion-resistant, maraging, and secondary hardening steel parts - SAE international, (n.d.).
Google Scholar
37. [37]
ASTM E8/E8M−22: standard test methods for tension testing of metallic materials, (n.d.).
Google Scholar
38. [38]
S. Trevor K, H. Zachary D, B. James T
Comparing stress corrosion cracking behavior of additively manufactured and wrought 17-4PH stainless steel
CORROSION, 78 (2022), pp. 528-546
Google Scholar
39. [39]
C. Fujii
Stress-corrosion cracking properties of 17-4 PH steel
stress Corros. Approaches, ASTM International, West Conshohocken, PA (1976), pp. 213-225, 10.1520/STP28681S
100 Barr Harbor Drive, PO Box C70019428-2959
Google Scholar
40. [40]
A. Barroux, N. Ducommun, E. Nivet, L. Laffont, C. Blanc
Pitting corrosion of 17-4PH stainless steel manufactured by laser beam melting
Corros. Sci., 169 (2020), Article 108594, 10.1016/j.corsci.2020.108594
View PDFView articleView in ScopusGoogle Scholar
41. [41]
Y.-H. Cho, S.-Y. Park, J.-Y. Kim, K.-A. Lee
17-4PH stainless steel with excellent strength–elongation combination developed via material extrusion additive manufacturing
J. Mater. Res. Technol., 24 (2023), pp. 3284-3299, 10.1016/j.jmrt.2023.03.228
View PDFView articleView in ScopusGoogle Scholar
42. [42]
Y. Weng, H. Dong, Y. Gan (Eds.), Advanced Steels: The Recent Scenario in Steel Science and Technology, Springer Berlin Heidelberg, Berlin, Heidelberg (2011), 10.1007/978-3-642-17665-4
Google Scholar
43. [43]
K. Li, S. Sridar, S. Tan, W. Xiong, Effect of homogenization on precipitation behavior and strengthening of 17-4PH stainless steel fabricated using laser powder bed fusion, (n.d.).
Google Scholar
44. [44]
A. Pellegrini, F. Lavecchia, M.G. Guerra, L.M. Galantucci
Influence of aging treatments on 17–4 PH stainless steel parts realized using material extrusion additive manufacturing technologies
Int. J. Adv. Manuf. Technol., 126 (2023), pp. 163-178, 10.1007/s00170-023-11136-3

View in ScopusGoogle Scholar

45. [45]

E. Rahimi, A. Rafsanjani-Abbasi, A. Imani, S. Hosseinpour, A. Davoodi

Correlation of surface Volta potential with galvanic corrosion initiation sites in solid-state welded Ti-Cu bimetal using AFM-SKPFM

Corros. Sci., 140 (2018), pp. 30-39, 10.1016/j.corsci.2018.06.026

View PDFView articleView in ScopusGoogle Scholar

46. [46]

L. Liang, D. Sun, B. Ning, Y. Chen, Z. Dong

Effect of δ-ferrite on the corrosion resistance of the 9Cr high nitrogen heat-resistant martensitic-steel

Mater. Lett., 322 (2022), Article 132532, 10.1016/j.matlet.2022.132532

View PDFView articleView in ScopusGoogle Scholar

47. [47]

Y. Zhai, X. Guo, Y. He, Z. Li

Corrosion resistance and mechanical properties of electrodeposited Co-W/ZrO2 composite coatings

Int. J. Electrochem. Sci., 18 (2023), Article 100015, 10.1016/j.ijoes.2023.01.015

View PDFView articleView in ScopusGoogle Scholar

48. [48]

H.-S. Kim, H.B. Lee, J. Chen, C. Jang, T.S. Kim, G.L. Stevens, K. Ahluwalia

Effect of zinc on the environmentally-assisted fatigue behavior of 316 stainless steels in simulated PWR primary environment

Corros. Sci., 151 (2019), pp. 97-107, 10.1016/j.corsci.2019.02.012

View PDFView articleView in ScopusGoogle Scholar

49. [49]

Y. Wu, D. Blaine, C. Schlaefer, B. Marx, R.M. German

Sintering densification and microstructural evolution of injection molding grade 17-4 PH stainless steel powder

Metall. Mater. Trans. A, 33 (2002), pp. 2185-2194, 10.1007/s11661-002-0050-4

View in ScopusGoogle Scholar

50. [50]

M. Saied, Experimental and numerical modeling of the dissolution of delta ferrite in the Fe-Cr-Ni system: application to the austenitic stainless steels, (n.d.).

Google Scholar

51. [51]

N. Saunders, U.K.Z. Guo, X. Li, A.P. Miodownik, J.-Ph. Schillé

Using JMatPro to model materials properties and behavior

JOM, 55 (2003), pp. 60-65, 10.1007/s11837-003-0013-2

View in ScopusGoogle Scholar

52. [52]

D. Alloyeau, G. Prévot, Y. Le Bouar, T. Oikawa, C. Langlois, A. Loiseau, C. Ricolleau

Ostwald ripening in nanoalloys: when thermodynamics drives a size-dependent particle composition

Phys. Rev. Lett., 105 (2010), Article 255901, 10.1103/PhysRevLett.105.255901

View in ScopusGoogle Scholar

53. [53]

P.W. Voorhees
The theory of Ostwald ripening
J. Stat. Phys., 38 (1985), pp. 231-252, 10.1007/BF01017860
View in ScopusGoogle Scholar
54. [54]
J.H. Yao, K.R. Elder, H. Guo, M. Grant
Theory and simulation of Ostwald ripening
Phys. Rev. B, 47 (1993), pp. 14110-14125, 10.1103/PhysRevB.47.14110
View in ScopusGoogle Scholar
55. [55]
W.M. Swift
Kinetics of MnS precipitate coarsening in 3pct Si-Fe sheet
Metall. Trans., 4 (1973), pp. 153-157, 10.1007/BF02649614
View in ScopusGoogle Scholar
56. [56]
X. Lou, P.L. Andresen, R.B. Rebak
Oxide inclusions in laser additive manufactured stainless steel and their effects on impact toughness and stress corrosion cracking behavior
J. Nucl. Mater., 499 (2018), pp. 182-190, 10.1016/j.jnucmat.2017.11.036
View PDFView articleView in ScopusGoogle Scholar
57. [57]
W.S.W. Harun, R.I.M. Asri, F.R.M. Romlay, S. Sharif, N.H.M. Jan, F. Tsumori
Surface characterisation and corrosion behaviour of oxide layer for SLMed-316L stainless steel
J. Alloys Compd., 748 (2018), pp. 1044-1052, 10.1016/j.jallcom.2018.03.233
View PDFView articleView in ScopusGoogle Scholar
58. [58]
H.R. Habibi Bajguirani
The effect of ageing upon the microstructure and mechanical properties of type 15-5 PH stainless steel
Mater. Sci. Eng. A, 338 (2002), pp. 142-159, 10.1016/S0921-5093(02)00062-X
View PDFView articleView in ScopusGoogle Scholar
59. [59]
M. Villa, F.B. Grumsen, F. Niessen, T. Dahmen, L. Cao, M. Reich, O. Kessler, X. Huang, M.A.J. Somers
Aging 17-4 PH martensitic stainless steel prior to hardening: effects on martensitic transformation, microstructure and properties
Materialia, 32 (2023), Article 101882, 10.1016/j.mtla.2023.101882
View PDFView articleView in ScopusGoogle Scholar
60. [60]
M. Murayama, K. Hono, Y. Katayama
Microstructural evolution in a 17-4 PH stainless steel after aging at 400°C
Metall. Mater. Trans. A, 30 (1999), pp. 345-353, 10.1007/s11661-999-0323-2
View in ScopusGoogle Scholar
61. [61]
C. Garcia-Cabezon, M.A. Castro-Sastre, A.I. Fernandez-Abia, M.L. Rodriguez-Mendez, F. Martin-

Pedrosa
Microstructure–Hardness–Corrosion performance of 17–4 precipitation hardening stainless steels processed by selective laser melting in comparison with commercial alloy
Met. Mater. Int., 28 (2022), pp. 2652-2667, 10.1007/s12540-021-01155-8
View in ScopusGoogle Scholar

62. [62]
M.A. Melia, H.-D.A. Nguyen, J.M. Rodelas, E.J. Schindelholz
Corrosion properties of 304L stainless steel made by directed energy deposition additive manufacturing
Corros. Sci., 152 (2019), pp. 20-30, 10.1016/j.corsci.2019.02.029
View PDFView articleView in ScopusGoogle Scholar

63. [63]
J. Suryawanshi, T. Baskaran, O. Prakash, S.B. Arya, U. Ramamurty
On the corrosion resistance of some selective laser melted alloys
Materialia, 3 (2018), pp. 153-161, 10.1016/j.mtla.2018.08.022
View PDFView articleView in ScopusGoogle Scholar

64. [64]
D. Itzhak, E. Aghion
Corrosion behaviour of hot-pressed austenitic stainless steel in H2SO4 solutions at room temperature
Corros. Sci., 23 (1983), pp. 1085-1094, 10.1016/0010-938X(83)90090-2
View PDFView articleView in ScopusGoogle Scholar

65. [65]
E. Otero, A. Pardo, M.V. Utrilla, E. Sáenz, F.J. Perez
Influence of microstructure on the corrosion resistance of AISI type 304L and type 316L sintered stainless steels exposed to ferric chloride solution
Mater. Charact., 35 (1995), pp. 145-151, 10.1016/1044-5803(95)00099-2
View PDFView articleView in ScopusGoogle Scholar

66. [66]
E. Otero, A. Pardo, M.V. Utrilla, E. Sáenz, J.F. Álvarez
Corrosion behaviour of aisi 304l and 316l stainless steels prepared by powder metallurgy in the presence of sulphuric and phosphoric acid
Corros. Sci., 40 (1998), pp. 1421-1434, 10.1016/S0010-938X(98)00047-X
View PDFView articleView in ScopusGoogle Scholar

67. [67]
D. Kong, X. Ni, C. Dong, L. Zhang, C. Man, J. Yao, K. Xiao, X. Li
Heat treatment effect on the microstructure and corrosion behavior of 316L stainless steel fabricated by selective laser melting for proton exchange membrane fuel cells
Electrochimica Acta, 276 (2018), pp. 293-303, 10.1016/j.electacta.2018.04.188
View PDFView articleView in ScopusGoogle Scholar

68. [68]
R.N. Clark, J. Searle, T.L. Martin, W.S. Walters, G. Williams
The role of niobium carbides in the localised corrosion initiation of 20Cr-25Ni-Nb advanced gas-cooled reactor fuel cladding

Corros. Sci., 165 (2020), Article 108365, 10.1016/j.corsci.2019.108365
View PDFView articleView in ScopusGoogle Scholar
69. [69]
S. Kumar, A. Kumar, R.Madhusudhan Vinaya, R. Sah, S. Manjini
Mechanical and electrochemical behavior of dual-phase steels having varying ferrite–martensite volume fractions
J. Mater. Eng. Perform., 28 (2019), pp. 3600-3613, 10.1007/s11665-019-04101-3
View in ScopusGoogle Scholar
70. [70]
K. Fushimi, K. Yanagisawa, T. Nakanishi, Y. Hasegawa, T. Kawano, M. Kimura
Microelectrochemistry of dual-phase steel corroding in 0.1 M sulfuric acid
Electrochimica Acta, 114 (2013), pp. 83-87, 10.1016/j.electacta.2013.09.162
View PDFView articleView in ScopusGoogle Scholar
71. [71]
W. Kuang, X. Wu, E.-H. Han
Influence of dissolved oxygen concentration on the oxide film formed on 304 stainless steel in high temperature water
Corros. Sci., 63 (2012), pp. 259-266, 10.1016/j.corsci.2012.06.007
View PDFView articleView in ScopusGoogle Scholar
72. [72]
J.R. Deepak, V.K. Bupesh Raja, G.S. Kaliaraj
Mechanical and corrosion behavior of Cu, Cr, Ni and Zn electroplating on corten A588 steel for scope for betterment in ambient construction applications
Results Phys, 14 (2019), Article 102437, 10.1016/j.rinp.2019.102437
View PDFView articleView in ScopusGoogle Scholar
73. [73]
S. Esmailzadeh, M. Aliofkhazraei, H. Sarlak
Interpretation of cyclic potentiodynamic polarization test results for study of corrosion behavior of metals: a review
Prot. Met. Phys. Chem. Surf., 54 (2018), pp. 976-989, 10.1134/S207020511805026X
View in ScopusGoogle Scholar
74. [74]
M.R. Stoudt, R.E. Ricker, E.A. Lass, L.E. Levine
Influence of Postbuild microstructure on the electrochemical behavior of additively manufactured 17-4 PH stainless steel
JOM, 69 (2017), pp. 506-515, 10.1007/s11837-016-2237-y
View at publisherView in ScopusGoogle Scholar
75. [75]
Z.D. Harris, T.K. Shoemaker, L.E. Singer, J.R. Scully, J.T. Burns
On the mechanistic origins of the increased hydrogen environment-assisted cracking susceptibility of AM 17-4 PH steel
15th Int. Conf. Fract (2023)
Atlanta, GA USA
Google Scholar

76. [76]
R.O. Ritchie
The conflicts between strength and toughness
Nat. Mater., 10 (2011), pp. 817-822, 10.1038/nmat3115
View at publisherView in ScopusGoogle Scholar
77. [77]
S. Huang, P. Kumar, C.W.J. Lim, J. Radhakrishnan, U. Ramamurty
Fracture behavior of PH15-5 stainless steel manufactured via directed energy deposition
Mater. Des., 235 (2023), Article 112421, 10.1016/j.matdes.2023.112421
View PDFView articleView in ScopusGoogle Scholar